

# Fat2 acts through the WAVE regulatory complex to drive collective cell migration during tissue rotation

Anna Julia Squarr,<sup>1\*</sup> Klaus Brinkmann,<sup>1\*</sup> Baoyu Chen,<sup>2</sup> Tim Steinbacher,<sup>3,4,5</sup> Klaus Ebnet,<sup>3,4,5</sup> Michael K. Rosen,<sup>2</sup> and Sven Bogdan<sup>1</sup>

<sup>1</sup>Institute for Neurobiology, University of Münster, 48149 Münster, Germany

<sup>2</sup>Department of Biophysics and Howard Hughes Medical Institute, University of Texas Southwestern Medical Center at Dallas, Dallas, TX 75390

<sup>3</sup>Institute-associated Research Group "Cell adhesion and cell polarity," <sup>4</sup>Institute of Medical Biochemistry, and <sup>5</sup>Center for Molecular Biology of Inflammation, University of Münster, 48149 Münster, Germany

Directional cell movements during morphogenesis require the coordinated interplay between membrane receptors and the actin cytoskeleton. The WAVE regulatory complex (WRC) is a conserved actin regulator. Here, we found that the atypical cadherin Fat2 recruits the WRC to basal membranes of tricellular contacts where a new type of planar-polarized whip-like actin protrusion is formed. Loss of either Fat2 function or its interaction with the WRC disrupts tricellular protrusions and results in the formation of nonpolarized filopodia. We provide further evidence for a molecular network in which the receptor tyrosine phosphatase Dlar interacts with the WRC to couple the extracellular matrix, the membrane, and the actin cytoskeleton during egg elongation. Our data uncover a mechanism by which polarity information can be transduced from a membrane receptor to a key actin regulator to control collective follicle cell migration during egg elongation. 4D-live imaging of rotating MCF10A mammary acini further suggests an evolutionary conserved mechanism driving rotational motions in epithelial morphogenesis.

## Introduction

Collective and directed cell movements are essential for diverse developmental processes in animals. Recent advances in live imaging and ex vivo culture conditions of *Drosophila melanogaster* ovaries have led to the discovery of a new type of morphogenetic movement that drives egg elongation during fly oogenesis (Haigo and Bilder, 2011; Bilder and Haigo, 2012). Elongating follicles, so-called egg chambers, rotate around their anterior–posterior (A-P) axis during the initial stages of oogenesis. As follicle cells migrate around their circumferential axis, they build up a polarized ECM (Haigo and Bilder, 2011). The planar-polarized ECM has been proposed to function as a molecular corset to restrict radial expansion and to force egg chamber elongation (Haigo and Bilder, 2011; Bilder and Haigo, 2012). Like the ECM, the basal actin cytoskeleton forms a corset composed of parallel actin bundles aligned perpendicular to the A-P axis. Thus, the timing and orientation of follicle rotation coincide with the formation of a planar polarized ECM and basal actin cytoskeleton.

Which molecules drive the global egg chamber rotation? Two recent studies unraveled an important role of the Arp2/3 complex–activating WASP family verprolin homologous (WAVE) and its interaction partner Ena/Vasodilator-stimulated

phosphoprotein (Ena/VASP) in egg chamber elongation, two known key actin regulators promoting single-cell migration in different systems (Cetera et al., 2014; Chen et al., 2014b). WAVE forms a heteropentameric complex, the WAVE regulatory complex (WRC), comprising the Abelson interacting protein Abi, Kette/Nap1, Specifically Rac1 associated protein 1 (Sra-1), and the Hematopoietic Stem Progenitor Cell 300 (HSPC300; Eden et al., 2002; Chen et al., 2010). The loss of either the WRC or its conserved interaction to Ena in *Drosophila* results in abnormally shaped, round eggs (Cetera et al., 2014; Chen et al., 2014b). In vivo membrane labeling using a Neuroglian-GFP trap revealed that migrating follicle cells form membrane protrusions extending in the direction of rotational movement (Cetera et al., 2014). WAVE and Ena are enriched at the tips of these membrane protrusions, and a model has been proposed in which WAVE defines the protrusive edge of each follicle cell and WAVE-dependent lamellipodia drive collective follicle cell migration (Cetera et al., 2014). Consistently, RNAi-mediated depletion of Abi in all follicle cells completely blocks egg chamber rotation (Cetera et al., 2014).

By contrast, less clear is how global tissue rotation is coordinated and how the directionality of migrating follicle cells as an epithelial sheet is controlled. Elongating egg chambers

\*A.J. Squarr and K. Brinkmann contributed equally to this paper.

Correspondence to Sven Bogdan: sbogdan@uni-muenster.de

Abbreviations used in this paper: A-P, anterior–posterior; PCP, planar cell polarity; SIM, structured illumination microscopy; WIRS, WRC interacting receptor sequence; WRC, WAVE regulatory complex.

© 2016 Squarr et al. This article is distributed under the terms of an Attribution–Noncommercial–Share Alike–No Mirror Sites license for the first six months after the publication date (see <http://www.rupress.org/terms>). After six months it is available under a Creative Commons License (Attribution–Noncommercial–Share Alike 3.0 Unported license, as described at <http://creativecommons.org/licenses/by-nc-sa/3.0/>).

always rotate perpendicular to the A-P axis, either clockwise or counterclockwise (Haigo and Bilder, 2011). Genetic studies in *Drosophila* have already revealed a close functional relationship between the ECM, cell adhesion receptors and actin dynamics during egg chamber elongation. Mutations in genes encoding components of basement membrane such as laminin, collagen IV, their receptors such as  $\beta$ PS integrin, and the receptor phosphatase Dlar and the loss of the atypical cadherin Fat2 result in a common round-egg phenotype (Gates, 2012). These mutations lead to a misorientation of the basal actin bundles (Viktorinová et al., 2009; Gates, 2012). However, not all of the round-egg mutants show a fully penetrant phenotype varying in the frequency of round eggs produced. For example, loss of *dlar* function results in a moderate phenotype with ~14% round eggs (Bateman et al., 2001). Mosaic analysis further revealed that Dlar acts nonautonomously to control the basal actin cytoskeleton polarization (Bateman et al., 2001). A similar nonautonomous requirement was found for several round egg genes such as *fat2/kugelei* (Viktorinová et al., 2009; Gates, 2012). Remarkably, only *fat2* mosaic egg chambers containing more than 60% mutant follicle cells show a disruption in the planar actin alignment in relation to the A-P axis (Viktorinová et al., 2009). Thus, the mutant cells seem to be dragged along by remaining wild-type cells. This also suggests that cell–cell interactions are required for tissue-level alignment of the basal actin filaments. Fat2 is indeed a transmembrane cell adhesion receptor that might function in contact-based cell–cell signaling as known for the related Fat protein, an important mediator of planar cell polarity (PCP) signaling in *Drosophila* wing and eye development. Like all members of the Fat cadherin subfamily *Drosophila* Fat2 contains a large extracellular region containing 34 cadherin repeats, one laminin A subunit G domain and five EGF motifs in the membrane proximal region that might mediate either heterophilic or homophilic interactions as recently demonstrated for rat Fat2 (Nakayama et al., 2002).

Given the disrupted planar-polarized basal actin cytoskeleton in *fat2/kugelei* mutants, it has been proposed that Fat2 might control an alternative PCP pathway in follicle cells (Bilder and Haigo, 2012). Localization studies with a GFP-tagged transgene further support this idea (Viktorinová et al., 2009; Gates, 2012). A Fat2-GFP transgene has been reported to localize at tricellular junctions in developing egg chambers until stage 5, and concomitant with the proposed onset of egg chamber rotation, Fat2 relocates to the lagging edge of cells (Viktorinová et al., 2009; Gates, 2012). However, recent live-imaging analyses demonstrate that egg chamber rotation begins much earlier, before an asymmetric localization of Fat2-GFP can be observed (Cetera et al., 2014). Thus, the relocalization of Fat2 seems not to be the instructive signal for directional follicle cell migration.

In mammalian cells, the most similar mammalian Fat2 orthologue (Fat1) localizes at the tips of membrane protrusions and cell–cell contacts, where it regulates junctional actin dynamics and cell polarity through Ena/VASP proteins (Moeller et al., 2004; Tanoue and Takeichi, 2004). The cytoplasmic tail of the *Drosophila* Fat2 protein, however, lacks all three EVH1 binding sites, which mediate Ena/VASP binding of mammalian Fat1, suggesting that *Drosophila* Fat2 might be linked to the actin cytoskeleton by an alternative pathway. We recently described a novel mechanism directly linking the WRC to diverse cell adhesion molecules, ion channels, and G-protein–coupled receptors (Chen et al., 2014a). All these transmembrane receptors contain a conserved peptide motif, the WRC interacting

receptor sequence (WIRS) that directly binds a conserved interaction surface on the WRC formed by the Sra-1 and Abi subunit (Chen et al., 2014a). In flies, disruption of the WIRS binding surface in Abi results in impaired photoreceptor axon targeting, defective egg morphology, and partial female sterility (Chen et al., 2014a). Here, we identify the atypical cadherin Fat2 as a novel WIRS ligand and explore a molecular pathway in which Fat2 and Dlar act through the WRC to control collective cell migration during *Drosophila* oogenesis.

## Results

### Follicle cells form two different types of WRC-dependent actin-rich protrusions driving collective cell migration during egg chamber rotation

Recent data indicate that egg chamber rotation requires WAVE-dependent protrusions at each follicle cell's leading edge (Cetera et al., 2014). However, imaging of the actin cytoskeleton of rotating egg chambers has been largely limited to fixed samples or protrusion dynamics were visualized in vivo by membrane markers (Haigo and Bilder, 2011; Cetera et al., 2014). To better understand WRC function in actin-driven cell protrusions during follicle cell migration, we used a LifeAct-EGFP transgene that enables the visualization of actin-rich protrusions of migrating follicle cells at high resolution. As previously reported, a polarized rotation of wild-type egg chambers can clearly be observed from stage 4 until the end of stage 8 when border cell migration starts (Video 1; He et al., 2011; Bilder and Haigo, 2012; Cetera et al., 2014). LifeAct-EGFP not only marks cortical F-actin but also highly accumulates at actin-rich protrusions (Fig. 1 A, arrowheads; and Video 2 A). Follicle cells migrate as an epithelial sheet forming thin filopodial protrusions at the cell front rather than sheet-like lamellipodial protrusions found in single migrating cells (Fig. 1 A, open arrowheads; and Video 2 A). Strikingly, the largest cell protrusions emerge predominantly at the tricellular junctions at the cell's leading edge (Fig. 1 A, closed arrowheads; and Video 2 A). Unlike the small filopodial protrusions that uniformly extend from the cell membrane, junctional protrusions form highly dynamic tails that propel against the direction of movement (Fig. 1 A, closed arrowheads; and Video 2, A and B). The length of these whip-like protrusions remarkably increases during egg chamber maturation, and they assume a flagella-like shape and dynamics at the end of stage 8, when rotations slow down (Fig. 1 B, closed arrowheads; and Video 2 C). Whip-like protrusions at junctional contacts also can be observed with a fluorescent F-actin probe based on the calponin homology domain of utrophin (Utr-CH; Burkel et al., 2007) expressed under the endogenous *spaghetti-squash* (*sqh*; Rauzi et al., 2010) promoter, suggesting that these structures are not an artifact of LifeAct-EGFP overexpression (Video 2 D). All protrusive actin structures of migrating follicle cells are highly labile and thus are poorly preserved by standard fixation methods (Fig. 1, C and C'). However, we found optimal preservation of acute wild-type egg chamber preparations after fixation without any subsequent permeabilization and washing steps (Fig. 1, D and D'). High resolution structured illumination microscopy (SIM) of fixed wild-type egg chambers stained with fluorescently labeled phalloidin reveals numerous long filopodial and whip-like protrusions as similarly observed in vivo (Fig. 1, D and D').

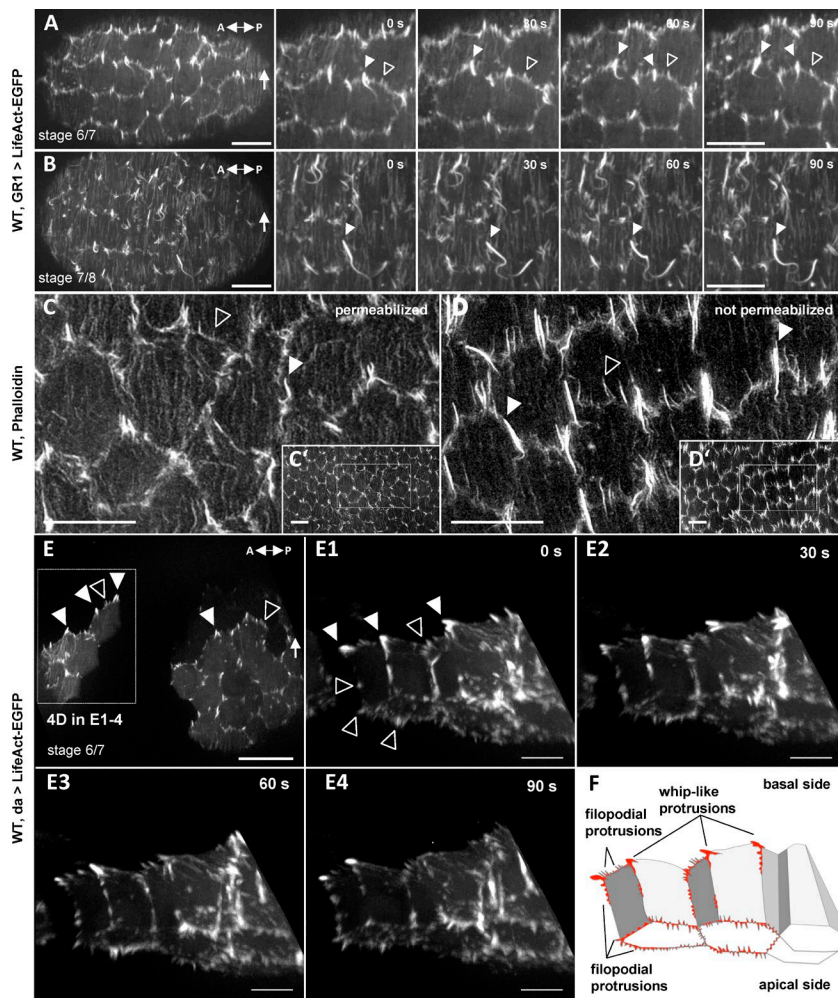


**Figure 1. Follicle cells form two different types of polarized actin-rich protrusions.** (A and B) Single frames of spinning disc microscopy time-lapse movies of ex vivo-cultured egg chambers expressing LifeAct-EGFP in the follicle epithelium using the GR1-Gal4 driver. Bars, 5  $\mu$ m. Stage 6/7 (A) and stage 7/8 egg chamber (B). Time intervals are indicated. Arrows mark the direction of collective cell migration. The closed arrowheads mark whip-like protrusions formed at tricellular junctions whereas open arrowheads in (A) mark smaller filopodial protrusions along the cell front. Cell protrusions extend in the same direction as follicle cell movement perpendicular to the A-P axis. See also Video 2, A–C. (C and D) SIM images from the basal surface of stage 6/7 wild-type follicle cells. Bars, 5  $\mu$ m. (C) Basal actin structures of follicle cells are poorly preserved by standard fixation methods. (D) Numerous filopodial and whip-like protrusions are preserved in acute preparations after fixation without any subsequent permeabilization and washing steps. C' and D' show entire SIM images, and the white boxes highlight the area of magnified insets shown in C and D. (E) Single frame of a spinning disc microscopy movie of an ex vivo-cultured egg chamber expressing LifeAct-EGFP in the follicle epithelium using the da-Gal4 driver. Arrows mark the direction of collective cell migration. The closed arrowheads mark whip-like protrusions, and open arrowheads mark smaller filopodial protrusions along the basal cell front and at the apical side. Bar, 10  $\mu$ m. See also Video 3 C. The white box marks the region selected for 4D reconstruction shown in (E1–4). Time intervals are indicated. Basal is up, and apical is down. Bars, 5  $\mu$ m. The closed arrowheads mark whip-like protrusions formed at tricellular junctions whereas open arrowheads mark smaller filopodial protrusions along the basal cell front and at the apical side. (F) Schematic drawing illustrates a 3D morphology of marked follicle cells in E4. WT, wild type.

To better visualize migration and protrusion dynamics of single follicle cells within the epithelium we made use of the da-Gal4 driver, which drives LifeAct-EGFP in a mosaic pattern (Fig. 1 E and Video 3, A and B). 4D live imaging analysis of thicker z-stacks through the mosaic follicle epithelium reveals that actin-rich filopodial protrusions are also visible along the baso-lateral cell border and at the apical side (Fig. 1 E and Video 3 C). In contrast to the basal side, filopodial protrusions at the apical side are not polarized along the migration direction but are rather radially symmetrical (Fig. 1, E1–E4; and Video 3 C). Whip-like protrusions are formed most basally or just beneath the basal surface at tricellular junctions (Fig. 1, E1–E4; and Video 3 C; compare scheme in Fig. 1 F). Both types of actin-rich protrusion, the filopodial and the junctional whip-like protrusions, depend on WRC function, because they are completely missing in *sra-1*-deficient follicle cells (Fig. 2 A and Video 4). Suppression of *sra-1* function also completely abolishes egg chamber rotation (see Fig. 6 G), confirming that WAVE-induced protrusions provide the driving force for follicle cell migration and egg chamber rotation (Cetera et al., 2014). Supporting this idea, *wave* and *abi* mutant cell clones completely lack actin-rich protrusions, large junctional and additionally cortical F-actin accumulations (Figs. 2 B and S1). Consistent with our previous studies, all WRC components are required for the integrity of the complex and the Abi protein level is strongly reduced in *wave* mutant cell clones (Stephan et al., 2011; Fig. 2 B). Mutant clones lacking the WRC show

no obvious defects in the formation or alignment of basal actin bundles as previously reported (Fig. 2 B, F-actin staining, asterisk; and Fig. S1 A; Viktorinová et al., 2009; Cetera et al., 2014). Thus, the remaining migrating wild-type cells might provide sufficient forces for cell migration driving the tissue-level based alignment of the actin cytoskeleton (Viktorinová et al., 2009; Horne-Badovinac, 2014).

#### The WRC accumulates at tricellular contacts in a Fat2-dependent manner

We next analyzed the localization of the central WRC component Abi in developing egg chambers. Consistent with the observation that the WRC is required for actin-rich protrusions of migrating follicle cells, the WRC subunit Abi indeed localizes at the right time and space in follicle cells. Endogenous Abi as well as an EGFP-tagged Abi transgene expressed in *abi* mutant follicle cells are highly enriched at dynamic protrusions emerging from tricellular junctions and along the membrane (Fig. 2, B and C; and Video 5 A). At later stages (9 and 10), follicle cells initiate oscillating acto-myosin contractions driving further egg chamber elongation (He et al., 2011). At this advanced stage of egg chamber maturation, when follicle cell migration ceases, the polarized localization of Abi changes into a more even distribution at basal cell-cell junctions (Fig. 2 D). Live-imaging analysis of stage 10 egg chambers expressing EGFP-tagged Abi documents these rhythmic cell contractions but also uncovers dynamic finger-like protrusions between follicle cells marked

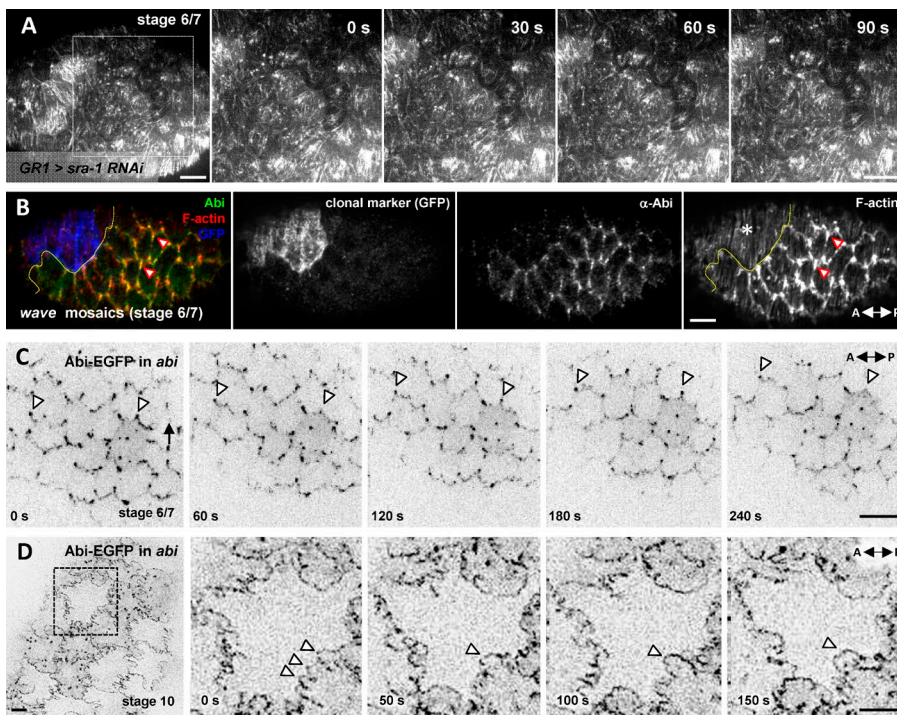


**Figure 2. Polarized actin-rich protrusions depend on WRC function.** (A) Follicle cell-specific RNAi-mediated knockdown of *sra-1* completely eliminates cellular protrusions. LifeAct-EGFP is more evenly distributed across the cell cortex. Time intervals are indicated. Bars, 5  $\mu$ m. (B) Confocal image from the basal surface of a wave mosaic egg chamber (stage 7) shows that mutant cells (positively marked by CD8-GFP expression, blue) completely lack actin-rich protrusions (F-actin, white) and endogenous Abi protein (green). The clonal border is marked with a yellow dotted line. In wild-type cells (EGFP-negative cells), Abi is enriched at actin-rich protrusions. The arrow shows the direction of the A-P body axis. The arrowheads highlight tricellular contacts where Abi and F-actin accumulate. The asterisk marks mutant cells with no obvious defects in the formation or alignment of basal actin bundles. (C) Spinning disc time-lapse series of an *abi* mutant egg chamber stage 6/7 reexpressing a GFP-tagged Abi rescue transgene. The arrowheads mark the enrichment of Abi at dynamic cell protrusions emerging from tricellular junctions. The arrow indicates the direction of migration. Bars, 5  $\mu$ m. See also Video 5 A. (D) Spinning disc time-lapse series of an *abi* mutant egg chamber stage 10 reexpressing an EGFP-tagged Abi rescue transgene. Dynamic finger-like protrusions between follicle cells are marked by Abi-EGFP (arrowheads). Bars, 5  $\mu$ m. See also Video 5 B.

by Abi-EGFP (Fig. 2 D, arrowheads; and Video 5 B). Genetic mosaics of stage 10 egg chambers lacking a functional WRC reveal an additional late function of the WRC in the organization or the maintenance of basal actin stress fibers mediating oscillating contractions (Fig. S1 B). *abi* mutant cell clones show a strong disorganization of basal actin bundles (Fig. S1 B), as previously described in clones deficient for the receptor tyrosine phosphatase Dlar (Bateman et al., 2001).

The prominent localization of the WRC at tricellular junctions resembles the distribution of Fat2 and Dlar reported previously (Bateman et al., 2001; Viktorinová et al., 2009). Because no specific anti-Fat2 antibody is available, we used a functional fosmid-based Fat2-GFP transgene (Viktorinová et al., 2009) to follow the localization of Fat2 with respect to the WRC in follicle cells. Structured illumination microscopy reveals an increasing overlap of Abi and Fat2-GFP at tricellular contacts in egg chamber development (Fig. 3, A–C; and Fig. S2). A reliable expression of Fat2-GFP is first seen in stage 3 follicle cells (Fig. 3 A). However, most prominent overlap of Abi and Fat2-GFP at tricellular contacts can be observed between stages 5 and 7 (Fig. 3, B and C; and quantification in Fig. 3, D and E). Live imaging of this weakly expressed Fat2-GFP confirms its accumulation at tricellular contacts of migrating stage 4/5 follicle cells (Video 6 A). Fat2-GFP remains enriched at tricellular contacts in vivo, although the initially weak expression signal increases over time, whereas Fat2-GFP becomes visible along the plasma membrane in stage 6–8 egg chambers (Fig. 3, F and G; and Video 6, A–C). Quantification of the relative GFP fluorescence intensity in living follicle cells confirms a significant accumulation of Fat2 at tricellular junctions between stages 5 and 9; the strongest localization at tricellular junctions is found at stage 6/7 (Fig. 3, F and G). In later stages, clones of follicle cells from stage 7/8 egg chambers expressing Fat2-GFP imply

an enrichment of Fat2 at the lagging edge as recently reported (Fig. S3; Viktorinová and Dahmann, 2013).

Co-labeling with LifeAct-RFP further shows a striking overlap of Fat2-GFP with junctional actin-rich protrusions in migrating follicle cells (Fig. 4 A and Video 7, A and B). Fat2-GFP localizes at the tips of whip-like protrusions (Fig. 4 B and Video 7, A and B).

### Fat2 is a novel WIRS ligand

The overlap of Fat2 with the WRC at tricellular junctions suggests that Fat2 might be involved in directing WRC-dependent follicle cell protrusions. Supporting this notion, the C-terminal intracellular tail of Fat2 (dFat2-CT) contains three highly conserved WIRS motifs that could mediate a direct interaction with the WRC (Fig. 4 C). A purified GST-fusion of dFat2-CT binds to the wild-type WRC, but not to a mutant whose WIRS binding surface is disrupted by mutations (Fig. 4 D; 2MBP-WRC AW). Binding assays with distinct double mutant C-terminal Fat2 proteins (WIRS  $\Delta$ 1, 2;  $\Delta$ 1, 3;  $\Delta$ 2, 3;  $\Delta$ 1, 2, 3; see loading control in Fig. 4 E, right) further revealed that the second and, to a lesser extent, the third WIRS motif are crucial for WRC binding (Fig. 4 E). Thus, Fat2 is a novel WIRS ligand.

Loss of WRC components affects egg shape (Cetera et al., 2014; Chen et al., 2014b). To test the functional relevance of the Fat2–WRC interaction in egg elongation, we first analyzed flies lacking the conserved WIRS binding surface in Abi (Abi $\Delta$ WIRS; Chen et al., 2014a). In these rescue experiments, we reexpressed either a wild-type Abi (Abi-WT) or a mutant Abi transgene bearing the two point mutations in the WIRS binding surface (Abi $\Delta$ WIRS, Abi-AW). In contrast to Abi-WT rescue, female flies deficient for WIRS binding (Abi $\Delta$ WIRS) show significant defects in egg shape (Fig. 5, A and B; Chen et al., 2014a). Quantifications by measuring the length-to-width

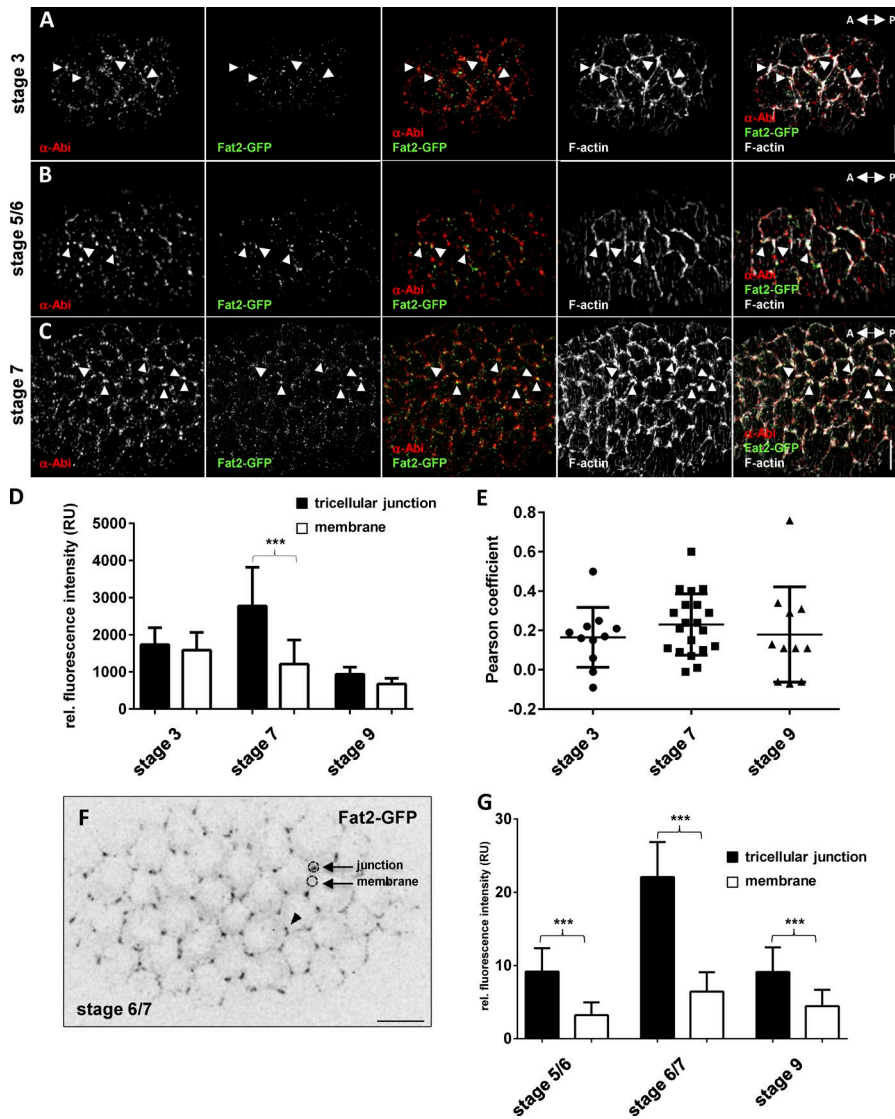


**Figure 3. Fat2 and WRC accumulate at tricellular junctions.** (A–C) Structured illumination microscopy (SIM) images from the basal surface of stage 3 (A), stage 5/6 (B), and stage 7 (C) egg chambers expressing a Fat2-GFP transgene. Fat2 (green), endogenous Abi (red), and actin-rich protrusions (F-actin, white) colocalize at tricellular junctions. Bars, 5  $\mu$ m. (D) Quantification of the relative Fat2-GFP signals (costained with an anti-GFP antibody) at tricellular contacts and along the membrane in fixed follicle cells confirms a significant accumulation of Fat2 at tricellular junctions. The strongest localization of Fat2 at tricellular junctions is found at stage 7. \*\*\*,  $P < 0.0001$  (ANOVA). Error bars represent mean  $\pm$  SD. (E) Colocalization analysis of Fat2 and Abi based on Pearson's colocalization coefficient. Fat2 and Abi shows the strongest overlap at tricellular contacts at stage 7. Triangles, circles, and squares represent single measurements of the Pearson's colocalization coefficient at indicated developmental stages. (F and G) Quantification of the relative Fat2-GFP fluorescence signals at tricellular contacts and along the membrane in living follicle cells as depicted in (F) confirms a significant accumulation of Fat2 at tricellular junctions from stages 5–9. Again, the strongest localization of Fat2 at tricellular junctions is found at stage 7. The fluorescence signal intensities were subtracted from the background signal. \*\*\*,  $P < 0.0001$  (ANOVA). Bars represent mean  $\pm$  SD. Bars, 5  $\mu$ m.

ratios revealed a bimodal phenotype. The majority shows a normal shape (Fig. 5 C), but  $\sim 20\%$  of all *Abi* $\Delta$ WIRS egg chambers are spherical as shown in Fig. 5 D. These 20% spherical egg chambers resemble the phenotype observed in *kugelei* mutants deficient for *fat2* (egg index  $< 2$ ; Fig. 5, A and D). In contrast, loss of *fat2* function or suppression of WRC subunits results in a fully penetrant round-egg phenotype (Fig. 5 A; Viktorinová et al., 2009; Cetera et al., 2014). The efficacy of RNAi-mediated knockdown depends not only on the transgenic line but also on the Gal4 driver used. As recently described, the GR1-Gal4 is expressed efficiently in follicle cells at all stages (Berns et al., 2014). Follicle cell-specific suppression of the WRC subunit *Sra-1* using the GR1-Gal4 driver results in the strongest round-egg phenotype, whereas RNAi-mediated downregulation of either *abi* or *wave* function results in a milder round-egg phenotype (Fig. 5 A; Cetera et al., 2014; Chen et al., 2014b). The level of gene activity suppression by transgenic RNAi also depends on the Gal4 driver. Supporting this notion, GR1-driven suppression of the WRC interaction partner *Ena* significantly affects egg elongation, whereas expression of the same *ena* RNAi transgene by the weaker TJ-Gal4 driver has no significant effect on egg shape as recently described (Fig. 5 A; Cetera et al., 2014).

Like *fat2* mutants, round *Abi* $\Delta$ WIRS stage 7–9 egg chambers show strong defects in the planar polarized basal follicle cell actin cytoskeleton (Fig. 5 E). Unlike *Abi*-WT rescued follicle cells, actin filaments are no longer aligned perpendicular to the A-P axis in *Abi* $\Delta$ WIRS egg chambers (Fig. 5 E). Analysis of actin bundle orientation documents strong orientation defects of actin bundles in *Abi* $\Delta$ WIRS and *fat2* mutant egg chambers (Fig. 5 F). The majority of actin bundles in *Abi* $\Delta$ WIRS and *fat2* mutant is not preferentially orientated perpendicular to the A-P axis ( $+90^\circ$ – $-90^\circ$ ) as observed for actin filament bundles in *Abi*-WT rescued follicle cells (Fig. 5, E and F). This suggests that egg chamber elongation requires not only the WRC and Fat2 but also functional WIRS interactions.

### Fat2 recruits the WRC to control planar polarized cell protrusions

Our previous data indicate that WIRS ligands can directly recruit the WRC to membranes (Chen et al., 2014a). To test whether the localization of the WRC depends on Fat2, we stained *fat2* mutant mosaic egg chambers for endogenous Abi. In contrast to wild-type cells (positively marked by GFP expression), in *fat2* mutant cells, Abi localization is strongly reduced at the basal follicle side (Fig. 6 A). Loss of *fat2* also substantially reduces

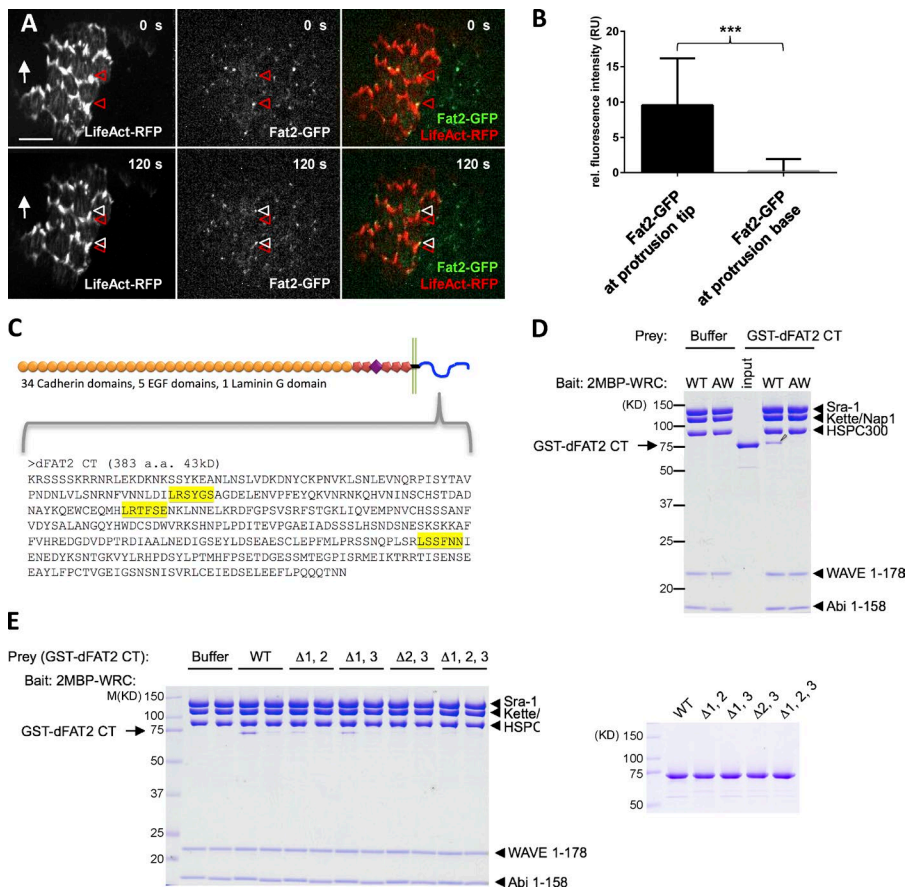


**Figure 4. Fat2 is a novel WRC ligand.** (A) Spinning disc time-lapse series of an egg chamber stage 5/6 coexpressing a LifeAct-RFP transgene under the da-Ga4 driver in Fat2-GFP background. The arrowheads mark the enrichment of Fat2-GFP at dynamic cell protrusions emerging from tricellular junctions over time. Red arrowheads mark beginning, white arrowheads mark position after 120 s. Bars, 5  $\mu$ m. (B) Quantification of the relative Fat2-GFP fluorescence signals at the tips versus the base of LifeAct-RFP-marked protrusions in migrating follicle cells. The fluorescence signal intensities were subtracted from the background signal. \*\*\*,  $P < 0.0001$  ( $t$  test). Bars represent mean  $\pm$  SD. (C) Schematic diagram of the molecular domain structure of the cadherin Fat2. Fat2 is a single-pass transmembrane cell adhesion receptor. The large extracellular region contains 34 cadherin repeats arrayed in tandem and in proximity to the membrane a laminin A subunit G domain and five EGF motifs. The sequence of the small intracellular C terminus, consisting of 383 amino acids (aa), contains three putative WIRS motifs, highlighted in yellow. (D) Coomassie blue-stained SDS-PAGE gel shows that immobilized *Drosophila* wild-type (WT) WRC, but not a mutant with a disrupted WIRS binding surface (AW for R118A/G122W-dAbi), selectively retained distinct GST-tagged fusions with the C terminus of *Drosophila* Fat2 (GST-dFat2 CT) containing distinct mutations of the three WIRS motifs, as highlighted in E. The relative position of the molecular weight markers in D are marked by black lines, based on their position in E (lane 1), which shows the same protein band pattern. (E, right) Loading control of the distinct GST-dFat2 CT fusion proteins.

actin-rich protrusions at the basal side (Fig. 6 A). Remaining protrusions show some residual Abi localization at tricellular contacts (Fig. 6 A, arrowheads). No changes in F-actin and Abi staining can be observed at baso-lateral cell membranes in the *fat2* mutant cells (Fig. 6 A, bottom). Because neither loss of the WRC nor disruption of its interaction to Fat2 in Abi $\Delta$ WIRS egg chambers affects the localization of Fat2-GFP (Fig. S4), these data indicate that Fat2 acts upstream of the WRC to regulate the localization of the WRC, which might in turn control the formation of polarized cell protrusions.

We further analyzed possible changes in the protrusive behavior of follicle cells lacking either *fat2* function or the interaction between the WRC and Fat2 in vivo. The comparison of migrating wild-type (Fig. 6 B and Video 8 A) and non-migrating *fat2* depleted follicle cells (Fig. 6 C and Video 8 B) reveals striking differences. As shown, migrating wild-type follicle cells form preferentially cellular protrusions at the cell front and at tricellular junctions, but not at the cell back (Figs. 1 E and 6 B and Video 8 A). In contrast, *fat2*-depleted cells show a loss of tricellular protrusions and remaining filopodial protrusions are distributed among the cell membranes pointing in opposite directions (Fig. 6 C, arrowheads; and Video 8 B). Disruption of the WRC–Fat2 interaction phenocopies *fat2* (Fig. 6 D and Video 8 C). Those 20% round Abi $\Delta$ WIRS mutant egg chambers (already visible at stage 6/7) show a loss of whip-like protrusions and multiple nonpolarized filopodial protrusions. For a quantitative measure of this finding, we analyzed the numbers of filopodia emerging either perpendicular or along the A–P axis over 15 min as illustrated in Fig. 6 E. We

found that in Abi-WT rescued follicle cells, filopodia are preferentially formed at the cell front (Fig. 6 F). In contrast, Abi $\Delta$ WIRS mutant and *fat2*-depleted cells show a strongly reduced bias for protrusion orientation (Fig. 6 F). Concomitantly, the Abi $\Delta$ WIRS and *fat2* mutant cells completely failed to migrate, whereas Abi-WT rescued follicle cells migrate at  $\sim 0.5$   $\mu$ m/min, similar to wild-type cells (0.6  $\mu$ m/min; Fig. 6 G). The loss of polarized cellular protrusions in *fat2* and Abi $\Delta$ WIRS mutant follicle cells might explain their loss of rotational movement (Video 8 D). Supporting this notion, disruption of polarized protrusions in wild-type egg chambers adhered on concavalin A-coated surfaces immediately blocks cell migration and egg chamber rotation (Video 9 A).

### The WRC physically and genetically interacts with Dlar

The finding that only 20% of the Abi $\Delta$ WIRS egg chambers exhibit an egg elongation defect implies additional regulatory mechanisms that enable Fat2 to act through the WRC on actin dynamics. The ECM binding receptor phosphatase Dlar might be part of this regulatory network, because loss of *dlar* function also results in a moderate round egg phenotype (Bateman et al., 2001). Supporting this notion, we found a similar overlap in the localization of endogenous Dlar and Abi throughout egg chamber development (Fig. 7 A). Interestingly, we found that Abi localization also depends on Dlar (Fig. 7). In *dlar* mutants, the localization of Abi is not as severely affected as in *fat2* mutants, but significantly reduced at the basal side (Fig. 7, compare A and B; C and D; and E and F). Compared

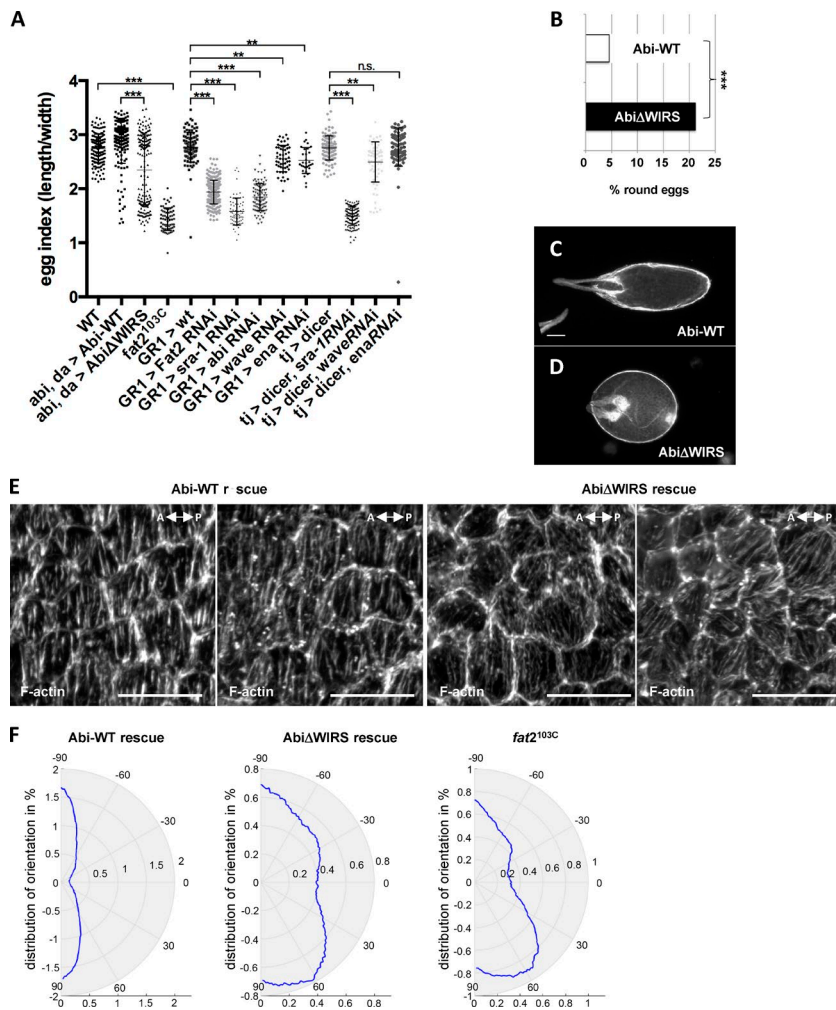


**Figure 5. Egg chamber elongation requires a functional WIRS.** (A) Quantification of egg morphology defects of indicated genotypes. Scatterplot shows the egg index which represents the quotient of length divided by width;  $n = 100$ . \*\*,  $P < 0.001$ ; \*\*\*,  $P < 0.0001$ ; and n.s., not significant (ANOVA). Please note that there are no significant differences between the wild-type and the Gal4 drivers alone. (B) Quantification of the frequency of round eggs of the two indicated genotypes. \*\*\*,  $P < 0.001$  ( $t$  test).  $n = 4$  independent experiments; in total, 1,304 wild-type eggs and 2,254 AbiΔWIRS eggs were analyzed. (C and D) Bright-field micrographs of *Drosophila* eggs of *abi* mutant females either rescued by reexpression of (C) a wild-type Abi (Abi-WT) transgene or (D) an Abi mutant transgene with a disrupted WIRS binding surface (AbiΔWIRS). Bars, 150  $\mu\text{m}$ . (E) Confocal images were taken from the basal surface of stage 7–8 egg chambers of indicated genotypes. F-actin was visualized with phalloidin. Bars, 10  $\mu\text{m}$ . (F) Quantification of the orientation of basal actin bundles in Abi-WT, AbiΔWIRS and *fat2* mutant egg chambers ( $n = 13$ ). Rose plots show density distribution of local angles of actin bundles (calculated using OrientationJ). The measured angles range between  $-90^\circ$  and  $90^\circ$ . In wild type, basal actin bundles are orientated perpendicular to the A-P axis ( $-90^\circ$  and  $90^\circ$ ).

with *fat2* mutants, higher levels of endogenous Abi can be still detected at tricellular contacts (compare arrowheads in Fig. 7, B, D, and F, Abi staining). F-actin still accumulates at tricellular junctions, but actin-rich protrusions along the membrane are clearly reduced (Fig. 7, B, D, and F, F-actin, arrowheads). These effects on Abi localization and F-actin are only seen in egg chambers that are completely mutant for *dlar* or in large *dlar* mutant clones as inferred from our mosaic analysis (Fig. 8, A and B). The global alignment of contractile actin bundles in most *dlar* egg chamber mutants is not affected. Thus, the remaining protrusions in *dlar* mutants might be sufficient to drive global alignment in most cases. Consistently, loss of Dlar function results in a moderate round-egg phenotype (Fig. 8 C; Bateman et al., 2001). Remarkably, removal of one copy *abi* in *dlar* mutant background strongly enhances the round egg phenotype, indicating that Dlar and Abi functionally interact in egg elongation (Fig. 8 C). Dlar might act through Ena on Abi. Dlar directly binds and dephosphorylates Ena (Wills et al., 1999), which in turn binds the WRC to promote actin polymerization and single-cell migration (Chen et al., 2014b). Supporting this notion, a GST fusion of the Ena-binding domain of Dlar (D2 domain; Wills et al., 1999) can pull down Abi from a cell extract of *Drosophila* S2 cells (Fig. 8 D). These data suggest that Ena might provide an important link between the ECM, tricellular junctions, and the actin cytoskeleton in egg elongation (Fig. 8 E). Live-imaging analysis of mutant egg chambers lacking the conserved interaction between WRC and Ena

indeed revealed a complete loss of egg chamber rotation and the formation of multiple nonpolarized protrusions reminiscent of *fat2* or AbiΔWIRS filopodia (Video 9 B).

In summary, we identified the atypical cadherin Fat2 as a novel WRC interacting receptor and define a molecular pathway (Fig. 8 E) in which Fat2 acts through the WRC to induce the formation of polarized cellular protrusions that drive collective cell migration during *Drosophila* oogenesis.

## Discussion

What drives symmetry-breaking in collective follicle cell migration? By analogy with the conventional PCP signaling in the wing, previous studies have led to a model in which the asymmetric localization of Fat2 might be required for the polarization of the cytoskeleton (Viktorinová and Dahmann, 2013). However, recent data already revealed that egg chamber rotation begins much earlier, suggesting that the relocalization of Fat2 to the lagging edge in stage 6–8 egg chambers cannot be the instructive signal for directional follicle cell migration (Cetera et al., 2014). Our present data further support this assumption and indicate an important role of Fat2 at tricellular contacts that might serve as a signaling platform initiating the polarization of the actin cytoskeleton (Fig. 8 F). Our live-imaging analyses revealed that large actin-rich protrusions are formed at tricellular junctions where Fat2 and the WRC already accumulate at early

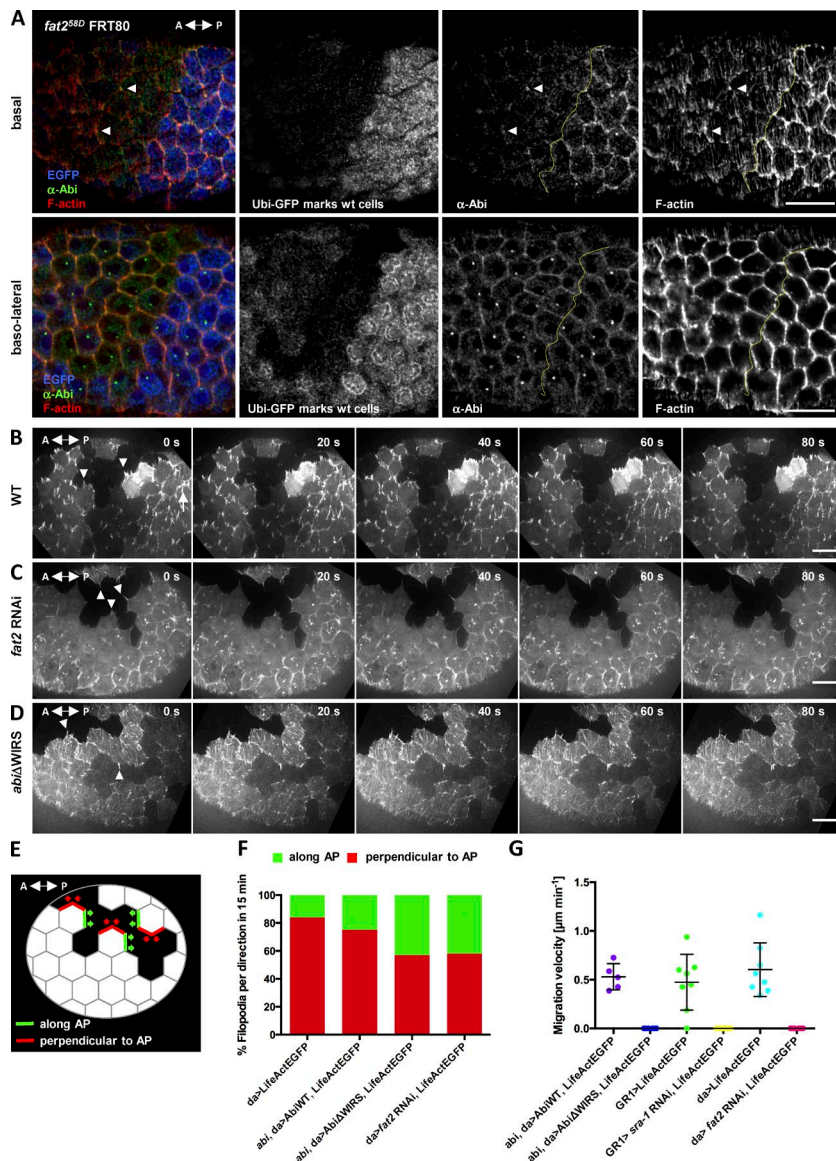


**Figure 6. Fat2 acts through the WRC to specify the protrusive leading edge of follicle cells driving global egg rotation.** (A) Confocal image from the basal surface of a *fat2* mosaic egg chamber (stage 7) shows that mutant cells (negatively marked by the absence of the ubi-EGFP marker, blue) show strongly reduced actin-rich protrusions (F-actin, white). In *fat2* mutant cells, endogenous Abi protein (green) is no longer enriched at the basal surface (top). However, Abi is still present at the baso-lateral region (bottom). The clonal border is marked by a yellow dotted line. The arrow shows the direction of the A-P body axis. Bars, 10 μm. (B–D) Single frames of spinning disc microscopy time-lapse movies of ex vivo-cultured ovarioles expressing LifeAct-EGFP in mosaic pattern (da-Gal4 driver). Time intervals and A-P axis direction are indicated. Bars, 5 μm. (B) Wild-type actin-rich cell protrusions are formed predominantly at tricellular junctions in the direction of the movement (arrowheads). (C) Nonmigrating follicle cells depleted for *fat2* or (D) lacking the WIRS interaction form more uniform cell protrusions, pointing into opposite directions (arrowheads). (E and F) Quantification of cell protrusions emerging either perpendicular (red) or along (green) the A-P axis over 15 min as depicted in E. Wild-type (six cell borders of each in four independent experiments) or Abi-WT (six cell borders of each in five independent experiments) follicle cells preferentially form filopodia at the cell front perpendicular to the A-P axis (red, 75–85%). AbiΔWIRS (eight cell borders of each in four independent experiments) mutant and *fat2*-depleted cells (ten cell borders of each in five independent experiments) show a strongly reduced bias for protrusion orientation. (G) Quantification of follicle cell migration velocity of indicated genotypes ( $n = 5-13$ ). Each data point represents an individual egg chamber. Bars represent mean  $\pm$  SD.

stages of developing egg chambers. They strongly resemble the whip-like microtubule-dependent appendages called flagella found in algae or cilia on the surface of many cells. A recent study revealed that whip-like appendages are able to synchronize cell movements in the green alga *Volvox* solely through interactions with the fluid that surrounds them (Brumley et al., 2014). In follicle cells, whip-like protrusions might interact similarly with the ECM to synchronize directed cell migration and to drive this novel type of morphogenetic movement.

A similar rotational cell movement has been recently identified in cultured epithelial cysts (Tanner et al., 2012; Wang et al., 2013). Nonmalignant mammary gland cell lines such as MCF10A cells form in 3D matrix spherical cysts (acini), which undergo multiple rotations (Tanner et al., 2012). Remarkably, their rotational movements also correlate with the formation of a planar polarized actin cytoskeleton and the assembly of an endogenous laminin matrix (Tanner et al., 2012). Thus, rotational motions seem to be a general feature of epithelial cells during tissue morphogenesis. To analyze the protrusion dynamics that drive rotational motions during mammary acinar morphogenesis, we performed

4D live imaging of cultured MCF10A cells infected with a LifeAct-EGFP lentivirus (Fig. 9 and Video 10). As recently reported, MCF10A cells form spherical cysts and undergo multiple rotations when cultured under spatially confined conditions (Tanner et al., 2012; Fig. 9 A and Video 10 A). Interestingly, we found that F-actin strongly accumulates at junctional interfaces at the basal side of rotating acini (Fig. 9, A and B; and Video 10, B and C). Similar to migrating follicle cells, rotating MCF10A acini form long actin-rich protrusions at basal intercellular junctions (Fig. 9, A and B; and Video 10, B and C). The similar morphology of the protrusions observed in rotating MCF10A acini suggests that the molecular mechanisms driving the tissue rotation are evolutionarily conserved. It is tempting to speculate that molecules such as human Fat2 homologue (Fat1) and Ena/VASP that are known to localize to filopodial protrusions and mature intercellular epithelial junctions might be part of the conserved molecular machinery driving rotational motions in epithelia (Moeller et al., 2004).

Different from all other round-egg genes identified so far, *fat2* encodes a cell-adhesion molecule of the cadherin subfamily. Fat2 might interact homophilically or might form

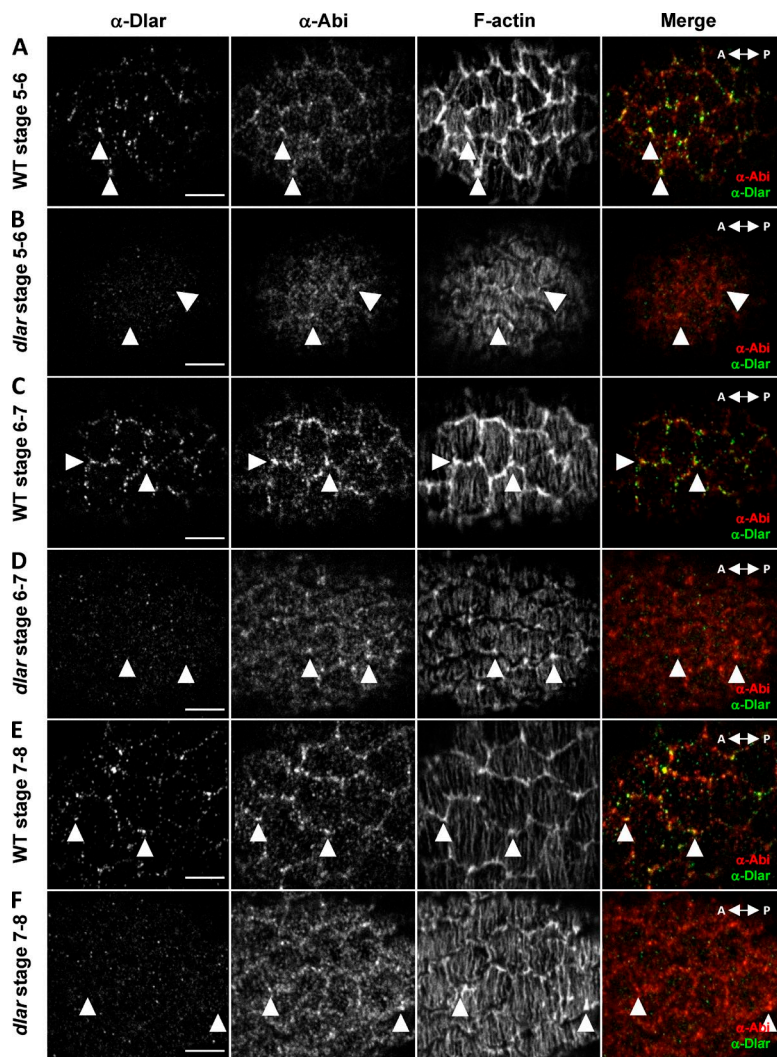


**Figure 7. Abi colocalizes with Dlar at tricellular contacts.** (A–F) Confocal images from the basal surface of developing wild-type (WT) and *dlar* (*dlar13.3/dlar5.5*) mutant egg chambers stained for endogenous Dlar, endogenous Abi, and F-actin (phalloidin). Stages are indicated. Bars, 5  $\mu$ m. The arrowheads mark tricellular contacts where Dlar and Abi overlap. Note that in *dlar* mutant cells, endogenous Abi and F-actin can be still detected at tricellular contacts (B, D, and F, arrowheads), but overall, the signal intensity is clearly reduced.

heterodimers as previously demonstrated for rat Fat2 or mouse Fat1 and Fat4 (Nakayama et al., 2002; Badouel et al., 2015). These homophilic interactions might modulate the intercellular shear stress between follicle cells and therefore might contribute to the orientation of cell migration as recently demonstrated by stress microscopy of epithelial monolayers (Tambe et al., 2011). The large extracellular domain of Fat2 may also mediate heterophilic interactions. One possible binding partner or coreceptor of Fat2 could be the membrane receptor phosphatase Dlar that directly binds ECM components such as laminin and nidogen (O’Grady et al., 1998). Previous studies already demonstrated a reciprocal influence of Dlar and Fat2 on their localization at tricellular junctions (Viktorinová et al., 2009). Our data suggest that both pathways, Fat2–WRC and Dlar–Ena, are tightly linked and converge to the WRC. Consistently, loss of the Fat2–WRC interaction might be at least partially compensated by Dlar–Ena interactions, a pathway in which Dlar acts through Ena to recruit the WRC.

Further understanding of how Dlar and Ena functions are integrated within the Fat2–WRC regulatory pathway could provide insights into the common mechanism by which these conserved molecular machineries coordinate collective cell migration that might also drive elongation of other developing organs, including those in vertebrates.

## Materials and methods

### *Drosophila* genetics

The following strains were used: *w*<sup>1118</sup> (B1 6326), *act5C-Gal4*, *da-Gal4*, *GR1-Gal4* (B1 36287), *mata4-Gal4* (B1 7063), *TJ-Gal4* (provided by V. Riechmann, Heidelberg University, Mannheim, Germany), *tub-Gal4*, *hs-Flp* (B1 42725), *FRT40A scarΔ37* (B1 8754), *FRT40A tubP-Gal80* (B1 42725), *FRT80B ubiGFP* (B1 5630), *FRT82B tubP-Gal80* (B1 5135), *Fat2 RNAi* (B1 40888), *Dlar RNAi* (B1 43979), *Ena RNAi* (B1 39034), *Abi RNAi* (B1 36707), *Sra-1 RNAi* (B1 38294), *Wave RNAi* (B1 36121), *UAS-mCD8-GFP* (B1 5136), *UAS-LifeAct-EGFP* (Zobel and Bogdan, 2013), *fat2*<sup>103C</sup>, *FRT80B fat2*<sup>58D</sup> and *Fat2-GFP* (provided by C. Dahmann; Viktorinová and Dahmann, 2013; B1 indicates Bloomington Stock Center). *abiΔ20*, *FRT82B abiΔ20* were generated by imprecise excision of the *EY20423* transposon located in the *abi* gene (Stephan et al., 2011). Full-length Abi-WT and AbiΔWIRS fragments were amplified by PCR and cloned into Gateway Entry Vectors (pENTR D-TOPO; Invitrogen). The inserts were sequenced and subcloned into pUAS-attB-rfA, pUASp-attB-rfA, pUAS-attB-rfA-EGFP (*Drosophila* Genomics Resource Center) by LR in vitro recombination (Invitrogen) as previously described (Chen et al., 2014a). The UAS-Abi-EGFP, UAS-Abi-WT, and UAS-Abi-ΔWIRS transgenes were generated by the germline-specific ΦC31 integration (Bischof et al., 2007) into the M{3xP3-RFP.attP}ZH-68E landing site. pUAS-based

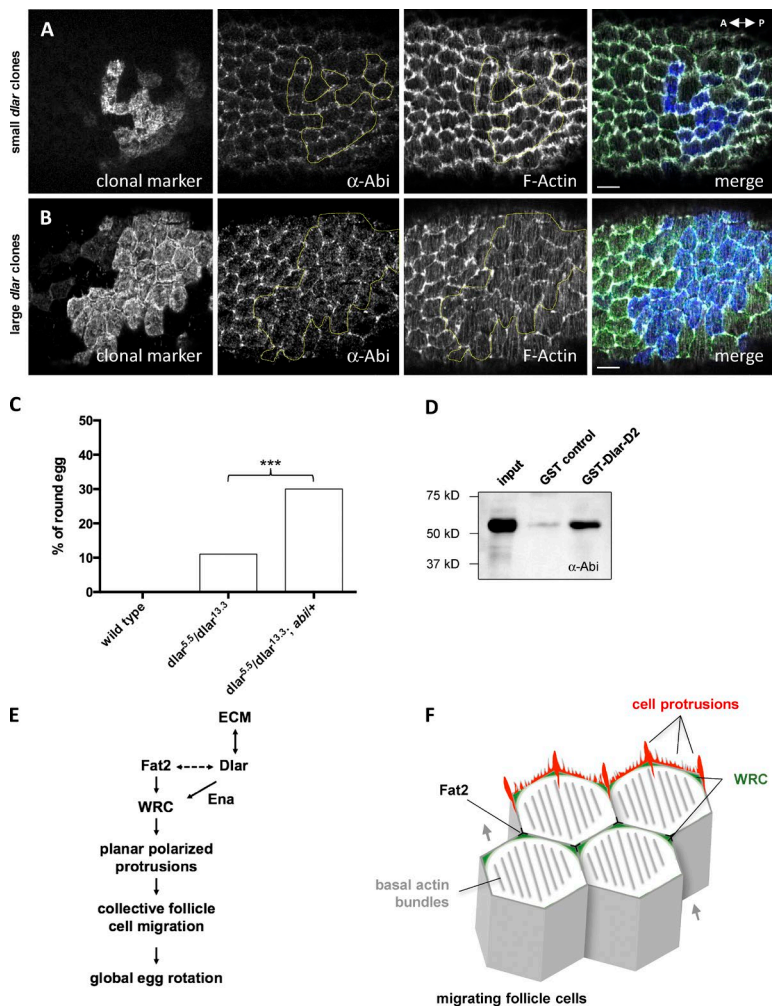


**Figure 8. Abi genetically and physically interacts with Dlar.** (A and B) Confocal images from the basal surface of *dlar<sup>5.5</sup>* (FRT40A) mosaic egg chambers (stage 7). (A) A small *dlar* mutant clone (positively marked by the presence of the CD8-GFP marker, blue) shows no changes of the actin cytoskeleton (F-actin, white), whereas (B) within a large *dlar* mutant clone, the basal actin-rich protrusions are strongly reduced. (C) Quantification of the frequency of round eggs of *dlar<sup>5.5</sup>/dlar<sup>13.2</sup>* ( $n = 314$ ) and *dlar<sup>5.5</sup>/dlar<sup>13.2</sup>;abi/+* ( $n = 257$ ) compared with wild type ( $n = 265$ ). \*\*\*,  $\chi^2 < 0.001$  ( $\chi^2$  test). (D) GST pull-down with GST-Dlar-D2 or GST coupled to glutathione beads incubated with extracts of S2 cells transfected with Abi. (E and F) Proposed model of how Fat2 acts through the WRC to drive collective cell migration during global egg rotation.

expression vectors were injected into an early embryo that incorporates the DNA into the germline. To identify positive integration events, the injected DNA carries besides its coding region additionally a marker gene. All *Drosophila* strains and crosses were performed at 25°C on standard medium. RNAi crosses were performed at 29°C.

### Clonal analysis

Marked clones of cells were generated by using the FLP-FRT system or the MARCM system (Lee and Luo, 2001). Cell clones for *fat2* were induced by crossing a null allele FRT80B *fat2<sup>58D</sup>*/TM6b to hs-Flp;FRT80B ubi-GFP/TM6b. Marked clones lacking *abi* were induced by crossing a null allele hs-Flp;FRT82B *abiΔ20*/TM6b (Stephan et al., 2011) to act5C-Gal4,UAS-mCD8-GFP/CyO;FRT82B *tubP*-Gal80/TM6b (positively marked mutant clones). Marked clones lacking *wave* were induced by crossing a null allele FRT40A *scarΔ37*/CyO<sup>twist-Gal4>UAS-GFP</sup>;TM2/TM6ubi<sup>GFP</sup> to hs-Flp;FRT40A-*tubP*-Gal80/CyO;tub-Gal4-UAS-mCD8-GFP/TM6b. Cell clones within the germline were induced by subjecting 1-d-old adult females to a 37°C heat shock (water bath) for 2 h in three successive days. After heat shock, flies had been placed in a fresh vial with yeast. Ovaries were dissected 1–2 d after the last heat shock.

### Immunohistochemistry

Antibody stainings were performed on ovaries dissected in *Drosophila* Schneider medium (Greiner), fixated for 15 min in 4% paraformaldehyde (Sigma-Aldrich) in PBS, permeabilized for 1 h in 0.1% Triton X-100 (Invitrogen) in PBS, blocked for 30 min in 3% BSA and stained with first antibody overnight at 4°C and for 2 h at RT with the second

antibody (Zobel and Bogdan, 2013). The following primary antibodies were used rabbit α-AbiA8 (1:1,000; this work), guinea pig α-WAVE (1:1,000; Bogdan et al., 2005), α-Dlar (1:500; DSHB), mouse α-GFP (1:1,000; Invitrogen). Secondary antibodies were Alexa Fluor 488- or 647-conjugated anti-rabbit, anti-guinea pig, and anti-mouse (Molecular Probes), all used at 1:1,000. F-actin was stained by either Alexa Fluor phalloidin 568 or Alexa Fluor phalloidin 488 (1:100; Invitrogen). Samples were mounted in Fluoromount (SouthernBiotech).

### Microscopy and live imaging of egg chambers

Light microscopic images of eggs were taken at an Axioplan 2 (Carl Zeiss) using a Plan-Neofluar 10×/0.30 objective. Fluorescently labeled specimens were analyzed on an AxioExaminer.Z1 microscope equipped with an LSM 710 confocal unit (Carl Zeiss) using a Plan-Apochromat 63×/1.4 oil-immersion objective. Further image processing was performed using the Zen 2009 software (Carl Zeiss). SIM images were taken with a CellObserver SD microscope equipped with ELYRA S.1 system using a 63×/1.4 oil-immersion objective (Carl Zeiss); five grid rotations were used with a mean of two as previously described. 4D datasets were analyzed using Imaris software (Bitplane).

Live imaging of egg chambers was performed in Schneiders medium (Sigma-Aldrich) containing 0.2 mg/ml insulin (Invitrogen) and 15% FCS (Thermo Fisher Scientific) at room temperature as previously described (Prasad et al., 2007), using an inverted Observer.Z1 microscope equipped with a Yokogawa CSU-X1 spinning disk scanning unit (YOKOGAWA), an Axiocam MRm CCD camera (6.45 μm × 6.45 μm; Carl Zeiss AG) and a 488-nm laser line (LAS

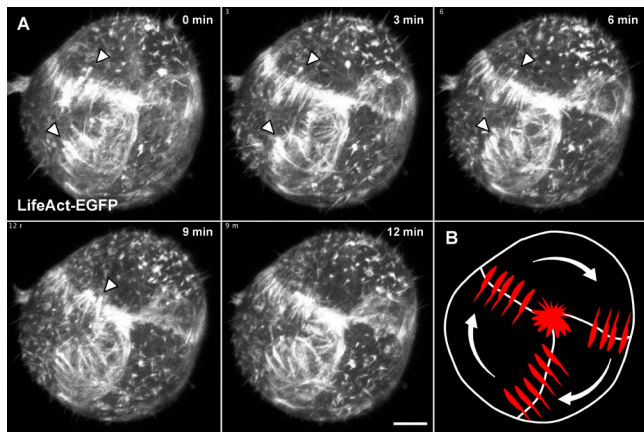


**Figure 9. Rotating MCF10A acini form polarized actin-rich protrusions.** MCF10A cells expressing LifeAct-EGFP were grown in a 3D basement membrane matrix for 2 d. (A) Confocal sections of a MCF10A acinus were taken at 3-min intervals as indicated. The LifeAct-EGFP signals are shown as maximum intensity projections from images acquired from the upper half of the acinus (see also Video 10 A for a 3D presentation of LifeAct-EGFP localization at time point 0). Arrowheads indicate dynamic actin protrusions. Actin dynamics recorded over a period of 40 min are shown in Video 10 B. Bars, 5  $\mu$ m. (B) Schematic representation of a rotating MCF10A acinus. White arrows indicate the direction of rotation, and actin protrusions are depicted in red. Note that tricellular corners are highly enriched for actin protrusions.

OS). Egg chambers were imaged through a Plan-Apochromat 25 $\times$ /0.8 (UV) Vis-IR oil-immersion objective, Plan-Apochromat 63 $\times$ /1.4 oil-immersion objective or Plan-Neofluar 100 $\times$ /1.30 oil-immersion objective (Carl Zeiss). ZEN software 2012 (Carl Zeiss) and Fiji (ImageJ) software was used for acquisition and processing of the images. Volume-rendered 4D reconstructions (gamma 1.0) were performed on the z-series (Fig. 1, E1–E4, and corresponding Video 7, A and B, were reconstructed based on 125 single sections over 15 min) was performed using Imaris software (Bitplane).

### Cultivation and lentiviral infection of MCF-10A cells

MCF-10A cells (provided by K. Matter, Institute of Ophthalmology, University College London, London, England, UK) were grown in DMEM/F12 (1:1) supplemented with 5% horse serum, 20 ng/ml EGF, 0.5  $\mu$ g/ml<sup>1</sup> hydrocortisone, 100 ng/ml cholera toxin, 10  $\mu$ g/ml insulin, 100 U/ml penicillin, and 100 U/ml streptomycin, as recently described (Debnath et al., 2003). MCF-10A cells expressing LifeAct-EGFP were generated using a lentiviral expression construct (LifeAct-EGFP in pFUGW; provided by H.-J. Schnittler, University of Münster, Münster, Germany). The LifeAct-EGFP plasmid was cotransfected with psPAX2 (virus-packaging plasmid) and pMD2G (envelope plasmid; 4:3:1 ratio) into Hek293T cells using X-Fect Transfection reagent (Clontech), as described previously (Tuncay et al., 2015). Cellular supernatants containing virus particles were harvested and used for MCF-10A infection. After overnight incubation, the virus containing culture medium was removed and the cells were cultivated in standard growth medium.

### 3D morphogenesis assay of MCF-10A mammary epithelial cells

Morphogenesis assays with MCF-10A cells were performed essentially as described elsewhere (Debnath et al., 2003). Briefly, MCF-10A cells were resuspended in assay medium (DMEM/F12 supplemented with 2% horse serum, 5 ng/ml EGF, 0.5  $\mu$ g/ml hydrocortisone, 100 ng/ml cholera toxin, 10  $\mu$ g/ml insulin, 100 U/ml penicillin, and 100 U/ml streptomycin). Eight-well chamber slides (Ibidi) were coated with 40  $\mu$ l growth factor reduced Geltrex (Thermo Fisher Scientific) per well. After

solidification of the matrix, 5  $\times$  10<sup>3</sup> cells in assay medium containing 2% Geltrex were seeded into each well. Acini were analyzed after 2–3 d using a confocal microscope (LSM 780; Carl Zeiss) equipped with an objective lens Plan-Apochromat 63 $\times$ /1.4 oil differential interference contrast (Carl Zeiss). 4D datasets were analyzed using Imaris software (Bitplane).

### Biochemical binding assay

MBP pull-down was performed as previously described (Chen et al., 2014a). In brief, 1 ml reactions containing 40 pmol 2MBP-tagged WRC, 400 pmol GST-dFAT2 CT, and 15  $\mu$ l amylose beads in binding buffer (20 mM Hepes, 100–120 mM NaCl, 5% [wt/vol] glycerol, 1 mM EDTA, and 5 mM  $\beta$ -mercaptoethanol, pH 7) were mixed at 4°C for 30 min. The beads were centrifuged and washed three times with the binding buffer. Bound proteins were eluted with 0.5% (wt/vol) maltose added in the binding buffer and examined by SDS-PAGE.

The Dlar-D2 domain (amino acids 1,191–1,480) was amplified by PCR, sequenced, and cloned into the pGEX-6P1 expression vector. GST-Dlar-D2 was expressed using *Escherichia coli* Arctic Express cells. Lysis was performed by sonification in (1 $\times$  PBS, 2 mM MgCl<sub>2</sub>, 2 mM DTT, 10% glycerol, and Protease Inhibitor Cocktail; Roche). After centrifugation GST-Dlar-D2 proteins were immobilized on glutathione resin according to the manufacturer's instructions (GE Healthcare). S2 cells transfected with pUAST-Abi and Act5c-Gal4 were harvested and lysed in 1 ml ice-cold lysis buffer (50 mM Tris, pH 7.4, 150 mM NaCl, 1 mM DTT, 1.5 mM MgCl<sub>2</sub>, 4 mM EDTA, 1% Triton X-100, 10% glycerol, and Protease Inhibitor Cocktail; Roche). After centrifugation, 500  $\mu$ l cytoplasmic supernatant was added to 50  $\mu$ l (GST-Dlar-D2 or GST-control) glutathione resin. After incubation for 1 h at RT, unbound proteins were washed away using four times 1 ml 1 $\times$  PBS. 20% of the preparation was used per lane on standard SDS-PAGE and analyzed by Western blot analyses.

### Statistical analysis

To quantify the egg index, the length and width of stage 14 eggs were measured manually. The quotient of length divided by width represents the egg index. For each genotype, 50–100 eggs were quantified. Each sample was tested for normal distribution using the Pearson d'Agostino Omnibus test. For statistical analysis of the egg index, an analysis of variance (ANOVA;  $P < 0.001$ ) was performed, when all samples were distributed normally. If one sample was not distributed normally, all samples were compared with the Kruskal-Wallis test ( $P < 0.001$ ) using PRISM software (GraphPad). The amount of round eggs produced by a certain genotype was counted manually (between 250 and 500 eggs depending on the genotype). Upon dissection, stage 14 eggs were sorted into two groups, round and elongated eggs. The number of each fraction was counted. The amount of each fraction in respect to the total number of eggs was given in percentage terms. The samples were compared statistically using the  $\chi^2$  test ( $\chi^2 = 0.001$ ), which compares the frequency distribution of two samples.

### Quantification of follicle cell migration velocity

Migratory speed of moving follicle cells was measured manually using Fiji software. One point of interest was set at a tricellular junction, which was followed over time. The distance between the resulting two points of interest was measured and the velocity was calculated according to distance per time ( $\mu$ m/min).

### Quantification of filopodia number and fluorescence intensities

The number of filopodia was counted manually over a time course of 15 min. Fluorescence intensities were measured using the Fiji software. The Pearson coefficient for tricellular junctions was measured using the coloc2 plug-in for Fiji software.

### Online supplemental material

Fig. S1 shows confocal images from the basal surface of *abi* mosaic egg chambers. Fig. S2 shows SIM images from the basal surface of progressively developing egg chambers expressing a Fat2-GFP transgene stained for endogenous Abi. Fig. S3 shows single frames of spinning disc microscopy time-lapse movies of ex vivo cultured stage 7/8 egg chambers expressing Fat2-GFP in a mosaic pattern. Fig. S4 shows SIM images from the basal surface of developing egg chambers expressing a Fat2-GFP transgene in *sra-1* RNAi and *AbiΔWIRS* background stained for endogenous Abi. Video 1 shows ex vivo-cultured wild-type ovarioles with rotating egg chambers (stage 7, 6, and stage 4/5) expressing LifeAct-EGFP in the follicle epithelium. Video 2 shows whip-like protrusions of migrating wild-type follicle cells expressing LifeAct-EGFP (GR1-Gal4) or Utrrophin-EGFP in developing egg chambers. Video 3 shows ex vivo-cultured egg chambers expressing LifeAct-EGFP in a mosaic pattern (*da-Gal4*) and a 4D movie of migrating wild-type follicle cells. Video 4 shows nonmigrating *sra-1*-depleted follicle cells (stage 7) expressing LifeAct-EGFP (GR1-Gal4). Video 5 shows two *abi* mutant egg chambers at different stages reexpressing an *Abi*-EGFP transgene (*da-Gal4*). Video 6 shows migrating follicle cells from egg chambers at different developmental stages expressing a Fat2-GFP transgene under the endogenous promoter. Video 7 shows migrating follicle cells expressing a Fat2-GFP transgene and LifeAct-RFP in a mosaic pattern (*da-Gal4* driver). Video 8 shows migrating wild-type follicle cells (stage 6/7) expressing LifeAct-EGFP in a mosaic pattern (*da-Gal4*) and movies of nonmigrating follicle cells (stage 6/7) either expressing a Fat2-RNAi transgene (*da-Gal4*) or lacking the WIRS interaction. Video 9 shows a wild-type egg chamber adhered to a concavalin A-coated surface and a movie of nonmigrating *abi* mutant follicle cells lacking the *Ena* interaction domain (stage 6/7). Video 10 shows rotational movement and 3D presentation of LifeAct-EGFP-infected MCF10A acini. Online supplemental material is available at <http://www.jcb.org/cgi/content/full/jcb.201508081/DC1>.

### Acknowledgments

We thank Ivana Viktorinova for helpful discussions and sharing unpublished data and Christian Klämbt and Meike Bechtold for helpful discussions and critical reading of the manuscript. We thank Hans-Joachim Schnittler for providing the lentiviral LifeAct-EGFP expression construct and Christian Dahmann for providing *fat2* mutant and Fat2-GFP stocks. We thank the Bloomington Stock Center, Vienna Drosophila RNAi Center, National Institutes of Genetics–Fly for fly stocks.

This work was supported by grants from the Deutsche Forschungsgemeinschaft to S. Bogdan (Heisenberg Program) and K. Ebnet (EB 160/4-2) and the Cells-in-Motion Cluster of Excellence [EXC 1003 – CiM], Westfälische Wilhelms-Universität Münster (to S. Bogdan).

The authors declare no competing financial interests.

Submitted: 20 August 2015

Accepted: 19 January 2016

### References

- Badouel, C., M.A. Zander, N. Liscio, M. Bagherie-Lachidan, R. Sopko, E. Coyaud, B. Raught, F.D. Miller, and H. McNeill. 2015. Fat1 interacts with Fat4 to regulate neural tube closure, neural progenitor proliferation and apical constriction during mouse brain development. *Development*. 142:2781–2791. <http://dx.doi.org/10.1242/dev.123539>
- Bateman, J., R.S. Reddy, H. Saito, and D. Van Vactor. 2001. The receptor tyrosine phosphatase Dlar and integrins organize actin filaments in the Drosophila follicular epithelium. *Curr. Biol.* 11:1317–1327. [http://dx.doi.org/10.1016/S0960-9822\(01\)00420-1](http://dx.doi.org/10.1016/S0960-9822(01)00420-1)
- Berns, N., I. Woichansky, S. Friedrichsen, N. Kraft, and V. Riechmann. 2014. A genome-scale in vivo RNAi analysis of epithelial development in Drosophila identifies new proliferation domains outside of the stem cell niche. *J. Cell Sci.* 127:2736–2748. <http://dx.doi.org/10.1242/jcs.144519>
- Bilder, D., and S.L. Haigo. 2012. Expanding the morphogenetic repertoire: perspectives from the Drosophila egg. *Dev. Cell.* 22:12–23. <http://dx.doi.org/10.1016/j.devcel.2011.12.003>
- Bischof, J., R.K. Maeda, M. Hediger, F. Karch, and K. Basler. 2007. An optimized transgenesis system for Drosophila using germ-line-specific phiC31 integrases. *Proc. Natl. Acad. Sci. USA.* 104:3312–3317. <http://dx.doi.org/10.1073/pnas.0611511104>
- Bogdan, S., R. Stephan, C. Löbke, A. Mertens, and C. Klämbt. 2005. Abi activates WASP to promote sensory organ development. *Nat. Cell Biol.* 7:977–984. <http://dx.doi.org/10.1038/ncb1305>
- Brumley, D.R., K.Y. Wan, M. Polin, and R.E. Goldstein. 2014. Flagellar synchronization through direct hydrodynamic interactions. *eLife*. 3:e02750. <http://dx.doi.org/10.7554/eLife.02750>
- Burkel, B.M., G. von Dassow, and W.M. Bement. 2007. Versatile fluorescent probes for actin filaments based on the actin-binding domain of utrophin. *Cell Motil. Cytoskeleton.* 64:822–832. <http://dx.doi.org/10.1002/cm.20226>
- Cetera, M., G.R. Ramirez-San Juan, P.W. Oakes, L. Lewellyn, M.J. Fairchild, G. Tanentzapf, M.L. Gardel, and S. Horne-Badovinac. 2014. Epithelial rotation promotes the global alignment of contractile actin bundles during Drosophila egg chamber elongation. *Nat. Commun.* 5:5511. <http://dx.doi.org/10.1038/ncomms6511>
- Chen, B., K. Brinkmann, Z. Chen, C.W. Pak, Y. Liao, S. Shi, L. Henry, N.V. Grishin, S. Bogdan, and M.K. Rosen. 2014a. The WAVE regulatory complex links diverse receptors to the actin cytoskeleton. *Cell*. 156:195–207. <http://dx.doi.org/10.1016/j.cell.2013.11.048>
- Chen, X.J., A.J. Squarr, R. Stephan, B. Chen, T.E. Higgins, D.J. Barry, M.C. Martin, M.K. Rosen, S. Bogdan, and M. Way. 2014b. *Ena*/VASP proteins cooperate with the WAVE complex to regulate the actin cytoskeleton. *Dev. Cell.* 30:569–584. <http://dx.doi.org/10.1016/j.devcel.2014.08.001>
- Chen, Z., D. Borek, S.B. Padrick, T.S. Gomez, Z. Metlagel, A.M. Ismail, J. Umetani, D.D. Billadeau, Z. Otwinowski, and M.K. Rosen. 2010. Structure and control of the actin regulatory WAVE complex. *Nature*. 468:533–538. <http://dx.doi.org/10.1038/nature09623>
- Debnath, J., S.K. Muthuswamy, and J.S. Brugge. 2003. Morphogenesis and oncogenesis of MCF-10A mammary epithelial acini grown in three-dimensional basement membrane cultures. *Methods.* 30:256–268. [http://dx.doi.org/10.1016/S1046-2023\(03\)00032-X](http://dx.doi.org/10.1016/S1046-2023(03)00032-X)
- Eden, S., R. Rohatgi, A.V. Podtelejnikov, M. Mann, and M.W. Kirschner. 2002. Mechanism of regulation of WAVE1-induced actin nucleation by Rac1 and Nck. *Nature*. 418:790–793. <http://dx.doi.org/10.1038/nature00859>
- Gates, J. 2012. Drosophila egg chamber elongation: insights into how tissues and organs are shaped. *Fly (Austin)*. 6:213–227. <http://dx.doi.org/10.4161/fly.21969>
- Haigo, S.L., and D. Bilder. 2011. Global tissue revolutions in a morphogenetic movement controlling elongation. *Science*. 331:1071–1074. <http://dx.doi.org/10.1126/science.1199424>
- He, L., X. Wang, and D.J. Montell. 2011. Shining light on Drosophila oogenesis: live imaging of egg development. *Curr. Opin. Genet. Dev.* 21:612–619. <http://dx.doi.org/10.1016/j.gde.2011.08.011>
- Horne-Badovinac, S. 2014. The Drosophila egg chamber—a new spin on how tissues elongate. *Integr. Comp. Biol.* 54:667–676. <http://dx.doi.org/10.1093/icb/icu067>
- Lee, T., and L. Luo. 2001. Mosaic analysis with a repressible cell marker (MARCM) for Drosophila neural development. *Trends Neurosci.* 24:251–254. [http://dx.doi.org/10.1016/S0166-2236\(00\)01791-4](http://dx.doi.org/10.1016/S0166-2236(00)01791-4)
- Moeller, M.J., A. Soofi, G.S. Braun, X. Li, C. Watzl, W. Kriz, and L.B. Holzman. 2004. Protocadherin FAT1 binds *Ena*/VASP proteins and is necessary for actin dynamics and cell polarization. *EMBO J.* 23:3769–3779. <http://dx.doi.org/10.1038/sj.emboj.7600380>
- Nakayama, M., D. Nakajima, R. Yoshimura, Y. Endo, and O. Ohara. 2002. MEGF1/*fat2* proteins containing extraordinarily large extracellular domains are localized to thin parallel fibers of cerebellar granule cells. *Mol. Cell. Neurosci.* 20:563–578. <http://dx.doi.org/10.1006/mcne.2002.1146>
- O’Grady, P., T.C. Thai, and H. Saito. 1998. The laminin-nidogen complex is a ligand for a specific splice isoform of the transmembrane protein tyrosine phosphatase LAR. *J. Cell Biol.* 141:1675–1684. <http://dx.doi.org/10.1083/jcb.141.7.1675>

- Prasad, M., A.C. Jang, M. Starz-Gaiano, M. Melani, and D.J. Montell. 2007. A protocol for culturing *Drosophila melanogaster* stage 9 egg chambers for live imaging. *Nat. Protoc.* 2:2467–2473. <http://dx.doi.org/10.1038/nprot.2007.363>
- Rauzi, M., P.F. Lenne, and T. Lecuit. 2010. Planar polarized actomyosin contractile flows control epithelial junction remodelling. *Nature.* 468:1110–1114. <http://dx.doi.org/10.1038/nature09566>
- Stephan, R., C. Gohl, A. Fleige, C. Klämbt, and S. Bogdan. 2011. Membrane-targeted WAVE mediates photoreceptor axon targeting in the absence of the WAVE complex in *Drosophila*. *Mol. Biol. Cell.* 22:4079–4092. <http://dx.doi.org/10.1091/mbc.E11-02-0121>
- Tambe, D.T., C.C. Hardin, T.E. Angelini, K. Rajendran, C.Y. Park, X. Serra-Picamal, E.H. Zhou, M.H. Zaman, J.P. Butler, D.A. Weitz, et al. 2011. Collective cell guidance by cooperative intercellular forces. *Nat. Mater.* 10:469–475. <http://dx.doi.org/10.1038/nmat3025>
- Tanner, K., H. Mori, R. Mroue, A. Bruni-Cardoso, and M.J. Bissell. 2012. Coherent angular motion in the establishment of multicellular architecture of glandular tissues. *Proc. Natl. Acad. Sci. USA.* 109:1973–1978. <http://dx.doi.org/10.1073/pnas.1119578109>
- Tanoue, T., and M. Takeichi. 2004. Mammalian Fat1 cadherin regulates actin dynamics and cell-cell contact. *J. Cell Biol.* 165:517–528. <http://dx.doi.org/10.1083/jcb.200403006>
- Tuncay, H., B.F. Brinkmann, T. Steinbacher, A. Schürmann, V. Gerke, S. Iden, and K. Ebnet. 2015. JAM-A regulates cortical dynein localization through Cdc42 to control planar spindle orientation during mitosis. *Nat. Commun.* 6:8128. <http://dx.doi.org/10.1038/ncomms9128>
- Viktorinová, I., and C. Dahmann. 2013. Microtubule polarity predicts direction of egg chamber rotation in *Drosophila*. *Curr. Biol.* 23:1472–1477. <http://dx.doi.org/10.1016/j.cub.2013.06.014>
- Viktorinová, I., T. König, K. Schlichting, and C. Dahmann. 2009. The cadherin Fat2 is required for planar cell polarity in the *Drosophila* ovary. *Development.* 136:4123–4132. <http://dx.doi.org/10.1242/dev.039099>
- Wang, H., S. Lacoche, L. Huang, B. Xue, and S.K. Muthuswamy. 2013. Rotational motion during three-dimensional morphogenesis of mammary epithelial acini relates to laminin matrix assembly. *Proc. Natl. Acad. Sci. USA.* 110:163–168. <http://dx.doi.org/10.1073/pnas.1201141110>
- Wills, Z., J. Bateman, C.A. Korey, A. Comer, and D. Van Vactor. 1999. The tyrosine kinase Abl and its substrate enabled collaborate with the receptor phosphatase Dlar to control motor axon guidance. *Neuron.* 22:301–312. [http://dx.doi.org/10.1016/S0896-6273\(00\)81091-0](http://dx.doi.org/10.1016/S0896-6273(00)81091-0)
- Zobel, T., and S. Bogdan. 2013. A high resolution view of the fly actin cytoskeleton lacking a functional WAVE complex. *J. Microsc.* 251:224–231. <http://dx.doi.org/10.1111/jmi.12020>

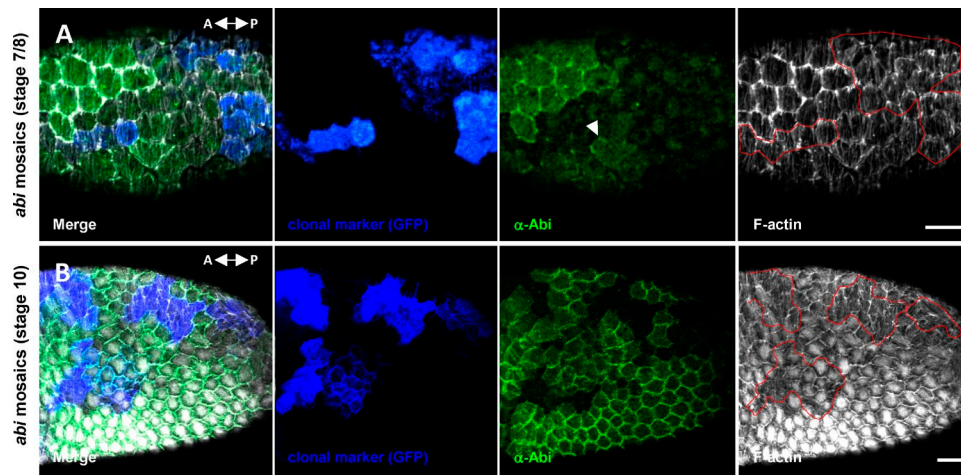
Squarr et al., <http://www.jcb.org/cgi/content/full/jcb.201508081/DC1>

Figure S1. **Loss of Abi function affects cell protrusions and the basal actin cytoskeleton in late mutant egg chambers.** (A) Confocal image from the basal surface of an *abi* mosaic egg chamber (stage 7/8) shows that mutant cells (positively marked by CD8-GFP expression, blue) completely lack actin-rich protrusions (F-actin, white) and endogenous Abi protein (green). The clonal border is marked with a red dotted line. In wild-type cells (GFP-negative cells) Abi is enriched at actin-rich protrusions at the cell front (arrow head). The anterior-posterior-body axis (A-P) is indicated. Bar, 10  $\mu$ m. (B) In late *abi* mosaic egg chambers (stage 10), the basal actin cytoskeleton (F-actin, white) is strongly reduced and disorganized in mutant cells (positively marked by CD8-EGFP expression, blue). The clonal borders are marked by red dotted lines. In wild-type cells (EGFP-negative cells), Abi localizes broadly to cell-cell junctions (Abi, green). Bar, 10  $\mu$ m.

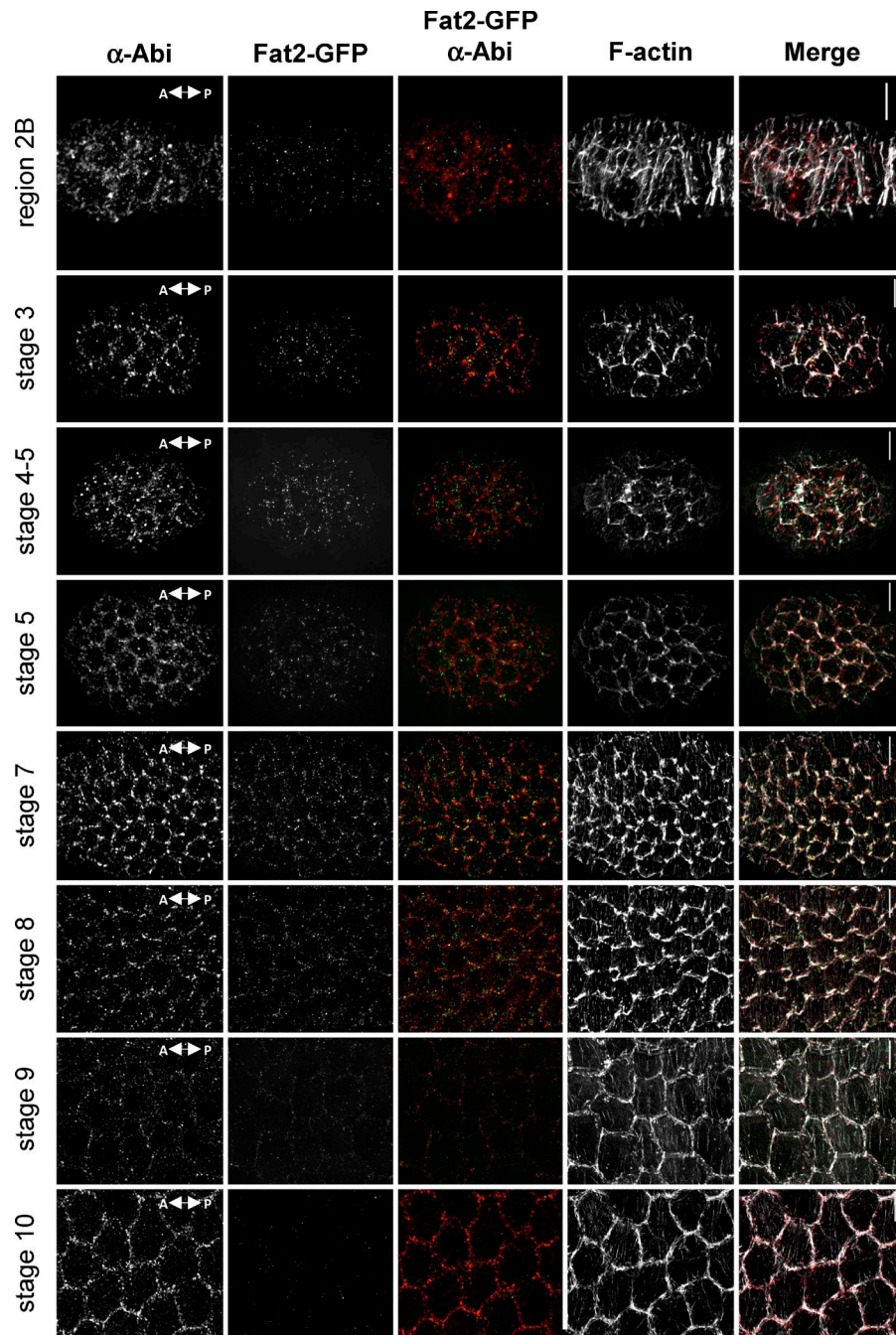


Figure S2. SIM images from the basal surface of progressively developing egg chambers expressing a Fat2-GFP transgene. Fat2 (green), endogenous Abi (red), and F-actin (white) are shown. Egg chamber stages and the A-P axis are indicated. Bar, 5  $\mu$ m.

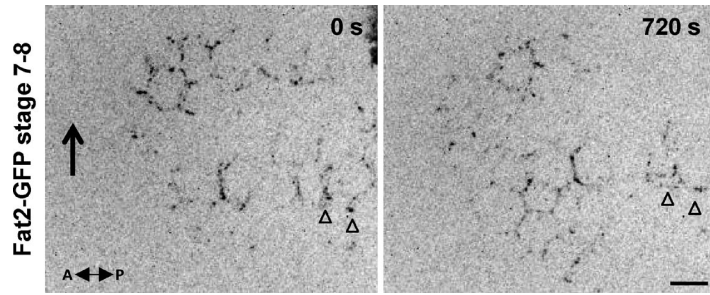


Figure S3. **Single frames of spinning disc microscopy time-lapse movies of ex vivo cultured stage 7/8 egg chambers expressing Fat2-GFP in a mosaic pattern.** Clonal expression was induced by heat-shock-induced expression of a flippase. Arrowheads mark the position of Fat2-GFP at the lagging edge of two migrating follicle cells. A-P axis is indicated. Bars, 5  $\mu$ m.

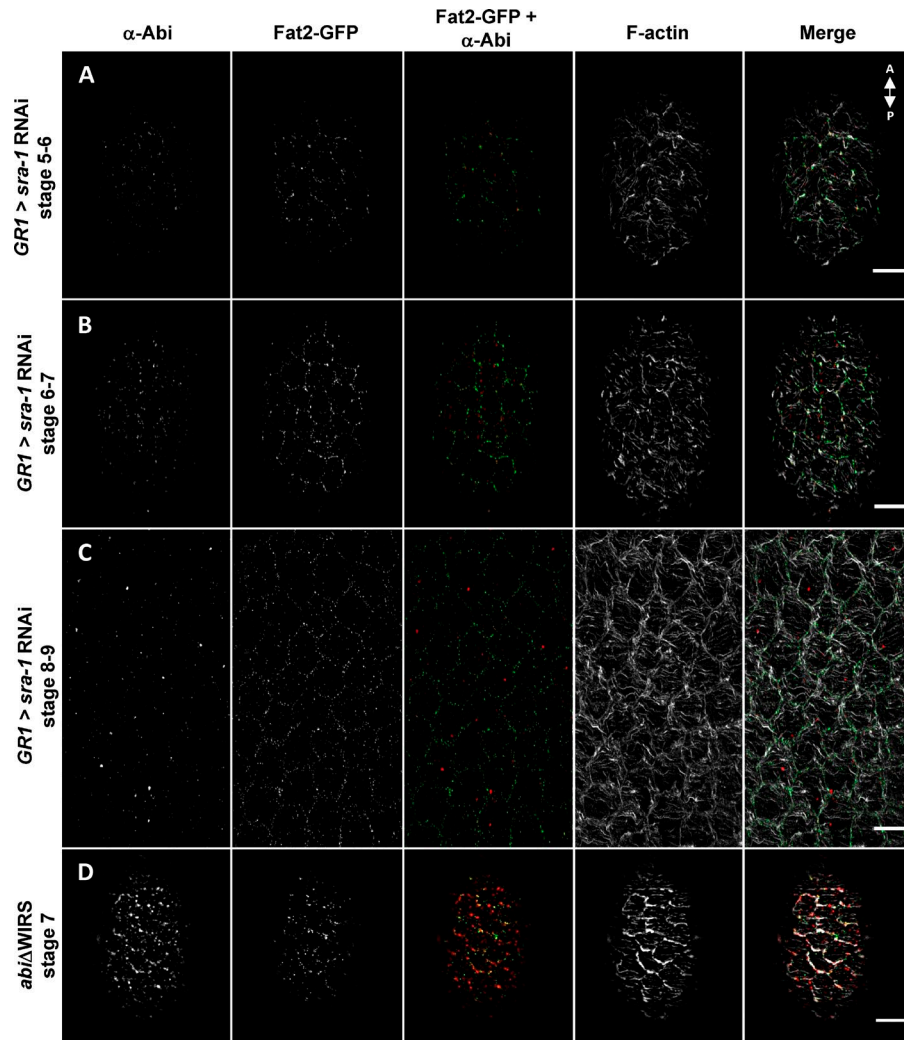
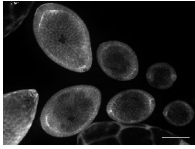
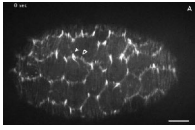


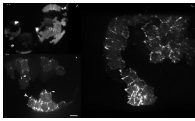
Figure S4. **Fat2 and Abi colocalizes at basal junctions of developing egg chambers.** (A–C) SIM images from the basal surface of developing egg chamber coexpressing a Fat2-GFP transgene and *sra-1* RNAi transgene under the GR1-Gal4 driver. Fat2 (green), endogenous Abi (red), and F-actin (white) are shown. (D) SIM image of a stage 7 egg chamber expressing a Fat2-GFP transgene in the *Abi* $\Delta$ WIRS background. Bar, 5  $\mu$ m.



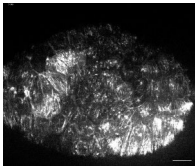
Video 1. **Spinning disc microscopy time-lapse movie of ex vivo-cultured wild-type ovarioles with rotating egg chambers (stage 7, 6, and 4/5) expressing LifeAct-EGFP in the follicle epithelium using the GR1-Gal4 driver.** Bar, 50  $\mu\text{m}$ .



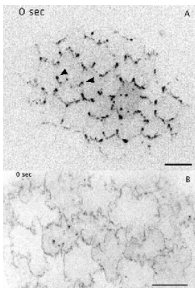
Video 2. **Follicle cells form two different types of polarized actin-rich protrusions.** (A–C) Spinning disc microscopy time-lapse movies of migrating wild-type follicle cells expressing LifeAct-EGFP in all follicle cells (GR1-Gal4). Stage 6/7 (A), stage 7 (B), and stage 7/8 (C) cells are shown. Closed arrowheads mark whip-like protrusions formed at tricellular junctions whereas open arrowheads mark smaller filopodial protrusions along the cell front. (D) Spinning disc microscopy time-lapse movie of ex vivo-cultured rotating wild-type egg chambers (stage 6/7) expressing Utrophin-EGFP under the endogenous *spaghetti-squash* (*sqh*) promoter in the follicular epithelium. Closed arrowheads mark whip-like protrusions formed at tricellular junctions. Bar, 5  $\mu\text{m}$ .



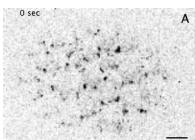
Video 3. **4D spinning disc microscopy reveals polarized cell protrusions at the basal side.** (A) Spinning disc microscopy time-lapse movie of ex vivo-cultured wild-type ovarioles with rotating egg chambers (stage 7, 6, and 4/5) expressing LifeAct-EGFP in a mosaic pattern (*da-Gal4*). (B) Spinning disc microscopy time-lapse movie of migrating wild-type follicle cells (stage 7) expressing LifeAct-EGFP in a mosaic pattern (*da-Gal4*). Closed arrowheads mark whip-like protrusions formed at tricellular junctions, whereas open arrowheads mark smaller filopodial protrusions along the cell front and the apical side. Bar, 5  $\mu\text{m}$ . (C) 4D spinning disc microscopy time-lapse movie of migrating wild-type follicle cells (stage 7) expressing LifeAct-EGFP in a mosaic pattern (*da-Gal4*).



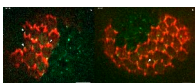
Video 4. **Spinning disc microscopy time-lapse movie of nonmigrating *sra-1* depleted follicle cells (stage 7) expressing LifeAct-EGFP under the control of the GR1-Gal4 driver.** Bar, 5  $\mu\text{m}$ .



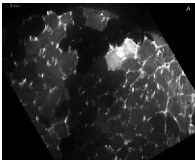
Video 5. **Spinning disc microscopy time-lapse movies of migrating *abi* mutant follicle cells reexpressing an Abi-EGFP transgene under the control of *da-Gal4* driver.** (A) Stage 7 egg chamber. (B) Stage 10 egg chamber. Bar, 5  $\mu\text{m}$ .



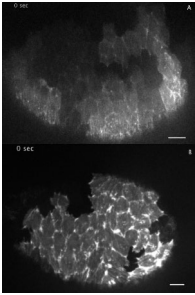
Video 6. **Spinning disc microscopy time-lapse movies of migrating follicle cells from egg chambers expressing a Fat2-GFP transgene under the endogenous promoter.** (A) Stage 4/5 egg chamber. (B) Stage 6/7 egg chamber. (C) Stage 7/8 egg chamber. Bar, 5  $\mu\text{m}$ .



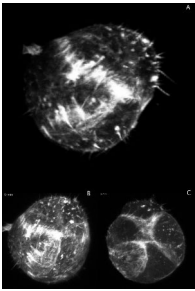
Video 7. **Spinning disc microscopy time-lapse movie of migrating follicle cells from egg chambers expressing a Fat2-GFP transgene and LifeAct-RFP in a mosaic pattern (*da-Gal4* driver).** (A) Stage 6/7 egg chamber. (B) Stage 7 egg chamber. Bar, 5  $\mu\text{m}$ .



Video 8. **Loss of Fat2 and WIRS interactions affects the protrusive behavior of follicle cells.** (A) Spinning disc microscopy time-lapse movie of migrating wild-type follicle cells (stage 6/7) expressing LifeAct-EGFP in a mosaic pattern (da-Gal4). (B) Spinning disc microscopy time-lapse movie of nonmigrating follicle cells (stage 6/7) expressing a Fat2-RNAi transgene. Transgenic expression of the RNAi construct and LifeAct-EGFP expression is driven by the da-Gal4 driver. (C) Spinning disc microscopy time-lapse movie of nonmigrating follicle cells lacking the WIRS interaction (stage 6/7). LifeAct-EGFP expression is driven by the da-Gal4 driver. (D) Spinning disc microscopy time-lapse movie of a nonrotating egg chamber lacking the WIRS interaction (stage 6/7). LifeAct-EGFP expression is driven by the da-Gal4 driver. Bar, 5  $\mu$ m.



Video 9. **Disruption of polarized cell protrusions blocks cell migration and egg chamber rotation.** (A) Spinning disc microscopy time-lapse movie of follicle cells taken from a wild-type egg chamber adhered to a concavalin A (ConA)-coated surface. Initial polarized filopodial protrusions are transformed into broad lamellipodial protrusions as similarly observed in *Drosophila* S2 cells when plated on ConA. (B) Spinning disc microscopy time-lapse movie of nonmigrating *abi* mutant follicle cells lacking the Ena interaction domain (stage 6/7). LifeAct-EGFP expression is driven by the da-Gal4 driver. Bar, 5  $\mu$ m.



Video 10. **Rotating cultured epithelial cysts form long actin-rich protrusions at basal intercellular junctions.** (A) 3D presentation of the upper half of a LifeAct-EGFP infected MCF10A acini generated by the Imaris software. Actin-based protrusions emerge from cell junctions basally and at tricellular vertices within the acinus. (B) Rotational movement of a MCF10A acinus composed of three cells. Actin dynamics visualized by LifeAct-EGFP are recorded over a period of 40 min. (C) Rotational movement of a MCF10A four-cell acinus. Actin dynamics visualized by LifeAct-EGFP are recorded over a period of 40 min.